Report
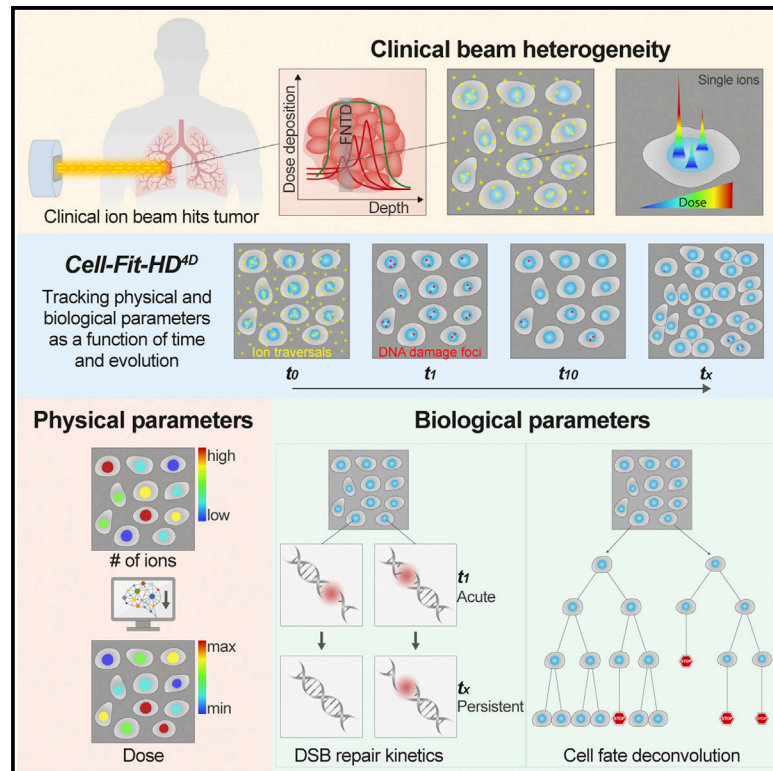
Biosensor for deconvolution of individual cell fate in response to ion beam irradiation

Graphical abstract

Highlights

- Cell-Fit HD⁴ᴰ is a biosensor that allows tracking of single irradiated cells

- The sensor correlates single-cell radiation dose with biological endpoints

- It also reveals variability in radiation responses in tumor cell population

- Potential to enhance understanding of therapeutic radiation dose concepts

Authors

Martin Niklas, Julian Schlegel, Hans Liew, ..., Oliver Jäkel, Jürgen Debus, Amir Abdollahi

Correspondence

m.niklas@dkfz.de (M.N.), j.schlegel@dkfz.de (J.S.)

In brief

Niklas et al. present Cell-Fit-HD⁴ᴰ, a biosensor that allows for microscopic tracking of fates and desired biological readouts in individual cells, in response to a therapeutically administered radiation dose. It has the potential to yield insights into the connection between dose deposition and cellular response in ion beam therapy.

CellPress

Report

Biosensor for deconvolution of individual cell fate in response to ion beam irradiation

Martin Niklas,[1,2,7,*] Julian Schlegel,[1,2,7,8,*] Hans Liew,[1,2] Ferdinand Zimmermann,[1,2] Katrin Rein,[1,2] Dietrich W.M. Walsh,[1,2] Oleh Dzyubachyk,[3] Tim Holland-Letz,[4] Shirin Rahmanian,[5] Steffen Greilich,[5] Armin Runz,[5] Oliver Jäkel,[2,5,6] Jürgen Debus,[1,2,6] and Amir Abdollahi[1,2,6]

[1]Division of Molecular and Translational Radiation Oncology and Clinical Cooperation Unit Translational Radiation Oncology, German Cancer Research Center (DKFZ) and Heidelberg University Hospital, 69120 Heidelberg, Germany
[2]National Center for Tumor Diseases, German Cancer Consortium, Heidelberg Institute of Radiation Oncology and National Center for Radiation Oncology, 69120 Heidelberg, Germany
[3]Department of Radiology and Department of Cell and Chemical Biology, Leiden University Medical Center, 2333 ZC Leiden, the Netherlands
[4]Division of Biostatistics, German Cancer Research Center (DKFZ), 69120 Heidelberg, Germany
[5]Division of Medical Physics in Radiation Oncology, German Cancer Research Center (DKFZ), 69120 Heidelberg, Germany
[6]Heidelberg Ion-Beam Therapy Center (HIT), Heidelberg, Germany
[7]These authors contributed equally
[8]Lead contact
*Correspondence: m.niklas@dkfz.de (M.N.), j.schlegel@dkfz.de (J.S.)
https://doi.org/10.1016/j.crmeth.2022.100169

MOTIVATION Ion beam cancer therapy (IBCT) is transforming radiotherapy into a highly precise discipline within oncology. Despite its promising clinical success, there is still a lack of understanding around the molecular and physiological changes in an individual tumor cell in response to the heterogeneous physical energy deposition in the ion beam. We therefore developed the biosensor "Cell-Fit-HD[4D]", enabling long-term monitoring of single tumor cells after clinical ion beam irradiation in combination with single-cell dosimetry. It enables correlation of physical beam parameters with biologically relevant endpoints in IBCT.

SUMMARY

Clonogenic survival assay constitutes the gold standard method for quantifying radiobiological effects. However, it neglects cellular radiation response variability and heterogeneous energy deposition by ion beams on the microscopic scale. We introduce "Cell-Fit-HD[4D]" a biosensor that enables a deconvolution of individual cell fate in response to the microscopic energy deposition as visualized by optical microscopy. Cell-Fit-HD[4D] enables single-cell dosimetry in clinically relevant complex radiation fields by correlating microscopic beam parameters with biological endpoints. Decrypting the ion beam's energy deposition and molecular effects at the single-cell level has the potential to improve our understanding of radiobiological dose concepts as well as radiobiological study approaches in general.
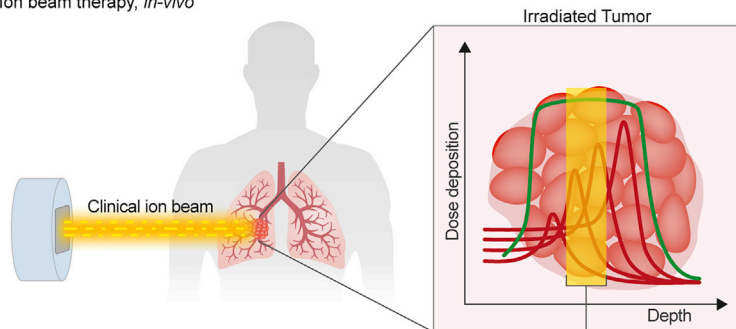
INTRODUCTION

Ion beam cancer therapy (IBCT) is transforming radiotherapy into a highly precise discipline within oncology (Marx, 2014). A Bragg peak enables precise deposition of a dose inside a tumor while sparing the surrounding healthy tissue (Jäkel, 2007; Schardt et al., 2010). Combining multiple ion beams, a "spread-out Bragg peak" (SOBP) is created, i.e., an extended region of uniform dose in depth on a macroscopic scale (Figure 1A). Heavy ions predominantly induce complex, persistent DNA double-strand breaks (DSBs; Karger and Peschke, 2017; Schardt et al., 2010; Siddiqui et al., 2015). Despite the promising clinical success of IBCT, there is still a great lack of understanding of the fundamental biological mechanisms that link the physical energy

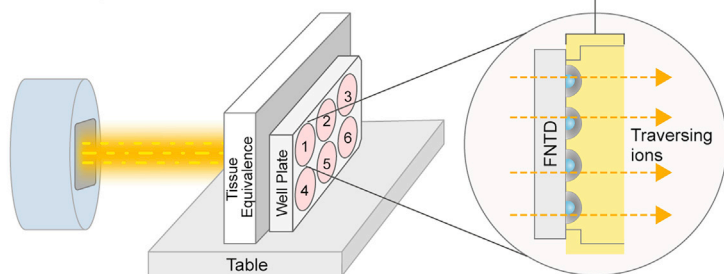deposition and the tumor response on molecular and higher scales.

On the cellular level, the dose applied in a SOBP is characterized by the entire spectrum of linear energy transfer (LET) and number of actual ion traversals, compared with the quasi-homogeneous photon dose (Schardt et al., 2010). As a consequence, cells in a given population not only receive a distribution of dose per cell, but different cells receiving the same physical dose can be exposed to a highly distinct number of ion traversals and LET combinations. Visualization and spatiotemporal correlation of the energy deposition in a tumor cell, combined with a readout of its fate in a clinical ion beam, would increase overall understanding of the relationship between energy deposition and biological response.
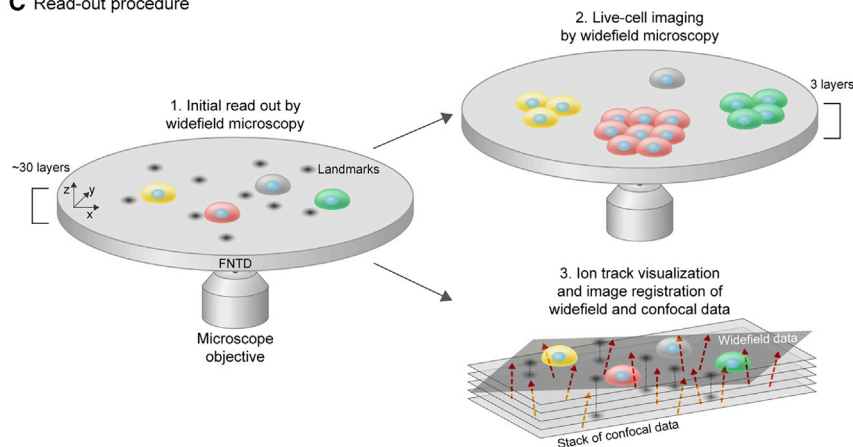
Figure 1. Cell-Fit-HD⁴ᴰ recapitulates the physical dose delivery of ion irradiation in tumor therapy

(A) By complex superposition of single Bragg peaks (red lines) a spread-out Bragg peak (SOBP, green line) is formed, enabling homogeneous dose deposition over the depth of the tumor volume. On a microscopic level, single tumor cells localized in a given plane (depicted by the yellow bar) are exposed to individual combinations of energies.

(B) The architecture and irradiation setup of *in vitro* biosensor Cell-Fit-HD⁴ᴰ mimics the clinical irradiation scenario of tumor cells in such a given plane. Irradiation setup was according to (Dokic et al., 2016).

(C) 1. In the initial readout, the so-called initial stack, the FNTD and the tumor cells are scanned in a single step. Thus, the earliest cellular response irradiation and the landmarks (indicated by black discs) for later image registration are recorded. 2. In a second step, imaging of the biological compartment is performed by widefield microscopy. 3. After imaging, the FNTD is read out by confocal microscopy. Using image registration, each ion track (arrows) can be reconstructed into the cell layer recorded in the initial readout.
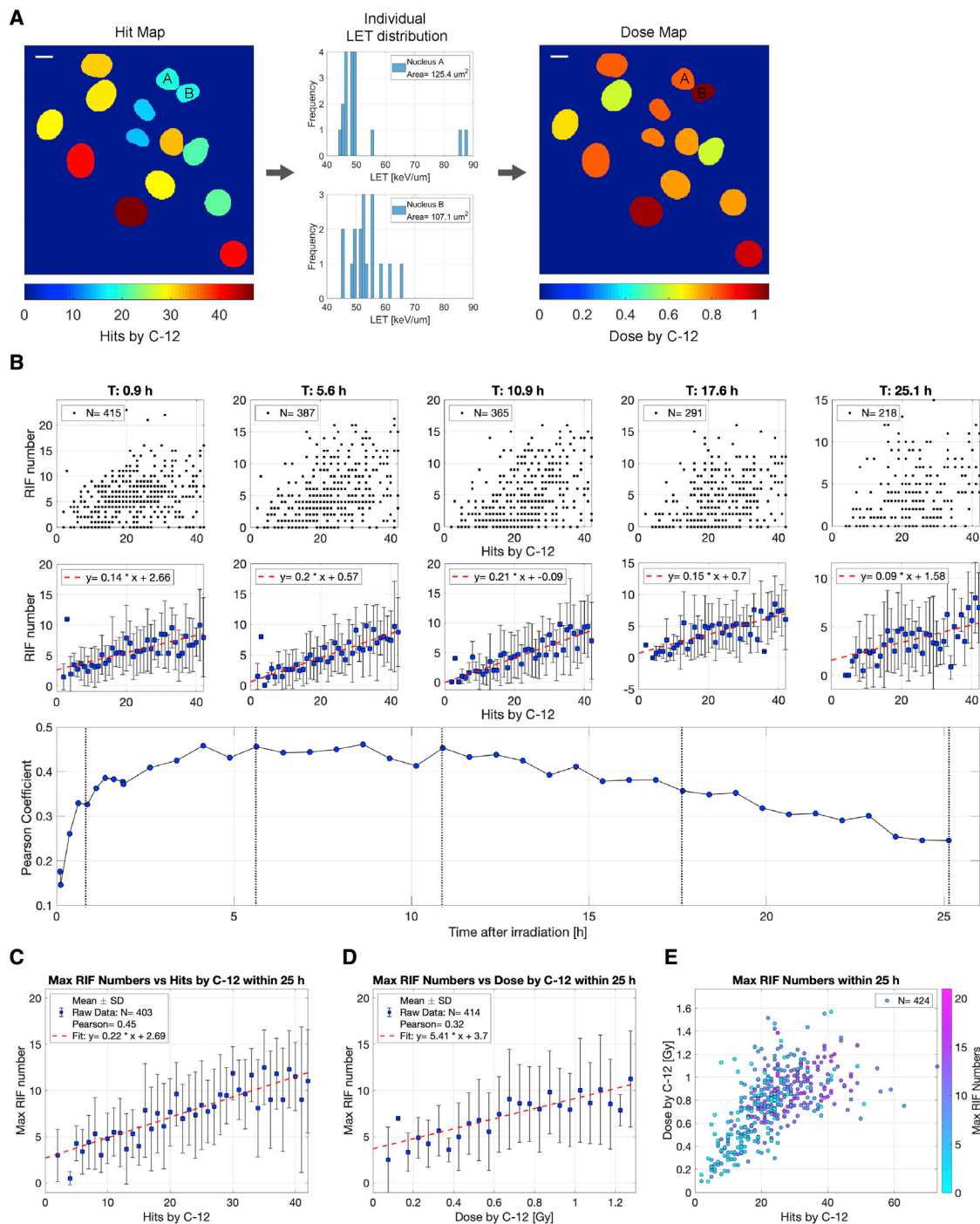
See also Figure S1.

HD) (Niklas et al., 2013a, 2013b, 2013c, 2016) to the fourth dimension: "Cell-Fit-HD⁴ᴰ". The setup in which Cell-Fit-HD⁴ᴰ is used mimics the clinical situation of a defined tumor depth during IBCT (Figure 1B). Cell-Fit-HD⁴ᴰ enables a complete deconvolution of the mechanisms linking the energy deposition of ions on the single-cell level with the ultimate and individual fate of heterogeneous tumor cells.

RESULTS

Architectures of Cell-Fit-HD⁴ᴰ

We engineered two architectures for Cell-Fit-HD⁴ᴰ. In the "wafer" architecture, cells (biological compartment) are seeded on top of the fluorescent nuclear track detector (FNTD, physical compartment), as for standard cell culture experiments (Figures S1A and S1B). This leads to a cell physiological condition suitable for long-term time imaging up to 5 days by wide-field microscopy (WFM), as indicated by typical proliferation curves (Figure S1C).

To overcome the limitations in using fluorescent dyes in the cell layer given by the excitation and emission spectra of the FNTD, we further developed the "mounting" architecture (Figure S1D). The rationale behind it is the spatial separation of the cell layer from the FNTD by a distance of ≥ 25 μm. It results in an improved signal-to-noise-ratio (SNR) of the readout signal of the cell layer: the ratio of mean recorded RIF number per cell nucleus 0.87 h after irradiation using the mounting and the wafer architecture was $\sim 4.39/3.24 = 1.35$ (Figure S1E).

Microbeams and CR-39 detectors have been used to study the effect of individual ion hits on single-cell fate (Chan et al., 2008; Friedland et al., 2019). Microbeam experiments are not yet capable of fully elucidating the response of cells in a clinical ion beam field due to the field's complex energy spectrum. The number of radiation-induced DNA damage foci (RIF) and their persistence in a cell nucleus have been used by others as a biological surrogate for the physical energy deposition in individual tumor cells (Belyaev, 2010). The recording and analysis of RIFs present at a single time point (TP), in turn, represents only a snapshot. It disregards the kinetics of DNA repair of individual cells triggered by the energy deposition in each individual cell.

We developed a biosensor that enables long-term monitoring of single tumor cells after clinical ion beam irradiation in combination with single-cell dosimetry. This extends our previously developed "cell-fluorescent ion track hybrid detector" (Cell-Fit-

Figure 2. Cell-Fit-HD[4D] allows for deconvolution of energy deposition (hits and dose by C-12 ions) in individual cell nuclei and correlation with RIF dynamics

(A) Cell nuclei derived from cell tracking and their hit numbers illustrated by color coding (left), as well as the LET distributions for nuclei A and B (middle), and the assessed dose level in the nuclei (right) are shown. Despite similar hit numbers, the corresponding dose level differs due to the individual LET distribution. Scale bars, 10 μm.

(B) Correlation between hits and RIFs at selected time points (TPs). Top row demonstrates the variability of RIF dynamics within a cell population. Middle row displays mean ± SD (errorbars) and demonstrates the positive correlation determined by linear regression analysis between hits and RIFs. Bottom graph displays the corresponding Pearson-r coefficient. Dashed lines indicate the TPs depicted above. The interval [5.6; 10.9]h post-irradiation RIF serves best as a surrogate for ion hits in single nuclei.

(legend continued on next page)

Both architectures enable the decoupling of the readout of the biological from the physical compartment—a key achievement (Figure 1C). The readout of the FNTD by confocal laser-scanning microscopy (CLSM) for ion track reconstruction is independent and can be carried out after recording of the cell layer.

Linear correlation of 53BP1 foci and deposited energy

We conducted several static as well as longitudinal measurements with carbon (C-12) ion-irradiated A549 cells using the wafer architecture.

The dose deposited in single-cell nuclei is mainly determined by the number of ion hits and the sum of their LETs. Measurements revealed the variability in hits based on a Poisson distribution. The variability in the deposited dose resulted from distinct numbers of ion hits with distinct LETs caused by the energy spectrum of the clinical SOBP (Figures 2A and S2A).

Whereas, as expected, the number of ion hits positively correlated with nucleus size (Pearson-r coefficient: 0.86), the dose did not (Pearson-r coefficient: −0.04; Figures S2B and S2C). The correlation between ion hits and dose in single nuclei could deviate substantially from linearity (Pearson-r coefficient: 0.31; Figure S2D).

Cell-Fit-HD^{4D} operates on single cells, the most fundamental biological, integer unit in radiation biology. We neglected the nucleus size and proposed the sum of single ions LET ($\sum$LET) as estimate for the deposited energy in single-cell nuclei. It was correlated with ion hits and dose: Pearson-r Coefficients of 0.94 and 0.48, respectively (Figures S2E and S2F).

Time-lapse microscopy and automated tracking of 53BP1-mCherry-expressing cells confers the possibility to correlate RIF dynamics with deposited energy on the single-cell level. We compared the correlations of RIF with hits and dose by linear regression analysis and calculation of Pearson-r coefficient within the first 25 h post-irradiation (Figures 2B and S2G). While we in principle observed a positive correlation with RIF number for both ion hits and dose, the data were characterized by substantial variability in the RIF evocation for single cells that received equal dose or hit numbers. The Pearson-r coefficient was found highest in the time interval between 5.6 and 10.9 h with values in the interval [0.42; 0.46] for hits and [0.29; 0.33] for dose. This time frame was further marked by maximum slopes in the interval of ∼ 0.2RIF/hit and ∼5.7RIF/Gy, respectively. Corresponding correlation to ΣLET is depicted in Figure S2H. Whereas the overall RIF number increased to maximum within the first hour (Figure S1E), only 2.6% of the nuclei displayed a RIF/hit ratio of ≥1.

Live-cell microscopy allowed us to assess the maximum RIF number (max RIF) observed in each individual cell. Introducing maximum RIF elevated the induction rate to 0.22RIF/hit and 5.41RIF/Gy (Figures 2C and 2D). We found that 75% of recorded cells showed the highest RIF numbers within 5.6 h, and 90% of the recorded cells showed the highest RIF numbers within 10.9 h (Figure S3A). Figures S3B and S3C show corresponding data for dose and $\sum$LET. Application of $\sum$LET did not further increase the Pearson-r coefficient: 0.39 compared with 0.45 for max RIF/hit correlation.

Clonogenic potential and growth arrest induction

Assessment of dose-dependent clonogenic survival is the gold standard for evaluation of radiation sensitivity. It is still not clear how energy deposition on the nuclear scale (Figures 2A–2F) in IBCT links to single-cell fate determination. To demonstrate the potential of the Cell-Fit-HD^{4D}, we tracked cells over a time period of >4 days and correlated their proliferative potential (total number of progeny cells originating from a single initial cell) to individually received ion hits. Although a certain tendency toward negative impact of the hit number on proliferation could be suspected, the data did not depict that the hit number directly translates to proliferative arrest in a quantitative manner (Pearson-r coefficient:-0.21; Figure 3A).

We assessed growth-arrest induction via p21 expression 4 days post-irradiation for individual cells (Figure 3B). We correlated p21 status to the proliferative potential of the mother cell, which revealed a binary distribution mirroring the binary readout of p21 positivity and negativity (Figures 3C and 3D). We plotted the parameters the p21 signal, proliferative potential, and ion hits for individual cells in one graph and defined quadrants based on the p21 positivity threshold and median hit number (median: 27; Figure 3E, for dose see Figure S3D). Cells from clonal lineages showing preserved proliferative potential predominantly expressed low p21 intensity (mean ≤ 66 a.u.), and rather received hit numbers in the range [10; 27]. Respective cell progeny constituted 54% of the experimental endpoint population. Above median hit numbers or dose did not necessarily limit clonogenic potential or induce p21, as more than 3/4 of the progeny of cells receiving the above-median hit numbers were determined to be p21 negative (comparing sectors II and III). Indeed, we could trace back lineages of single cells of interest and detect representative cases of differential cell fates in terms of subsequent proliferation and p21 expression following cell division (Figure 3F).

DISCUSSION

In contrast to existing radiation experiments, Cell-Fit-HD^{4D} combines single-cell dosimetry with individual tracking of a large number of cells for up to 5 days by live-cell imaging. This approach enables investigation of fundamental mechanisms linking the microscopic heterogeneous energy deposition to the response of individual tumor cells. We were able to start resolving the cell's individual response chain triggered by the physical energy deposition in its nucleus.

(C and D) Correlation of hits (C) and dose (D) with maximum detected RIF numbers (max RIF) within 25 h post-irradiation slightly improves linear regression. Respective Pearson-r coefficients demonstrate that max RIF shows higher correlation with received hits than with dose.

(E) Color-coded projection of max RIF on the combinatory patterns of hits and dose. Cells tend to develop more RIF if a distinct given dose is deposited by a higher number of ions. Each data point represents a single nucleus in B and E.

See also Figures S2 and S3.
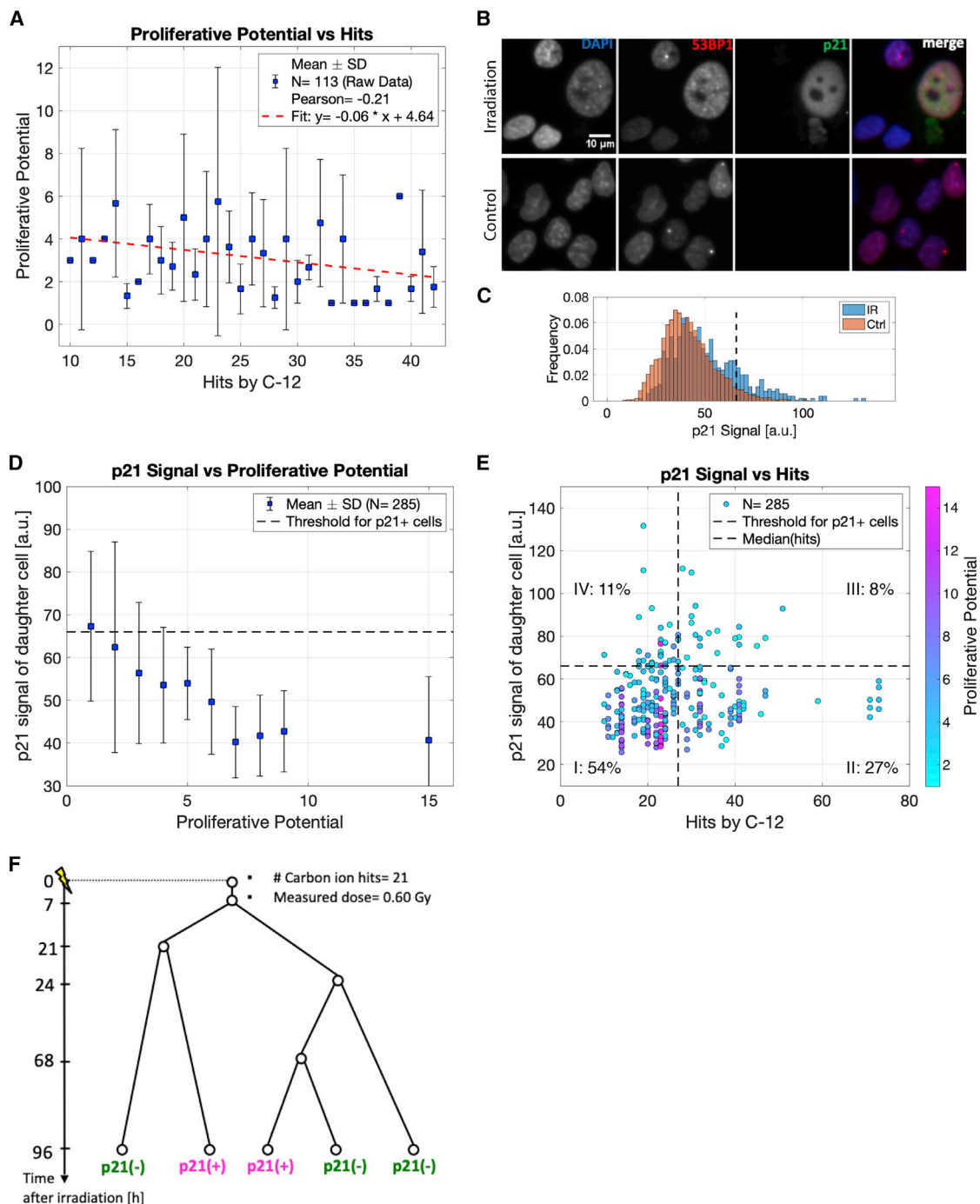
Figure 3. Cell-Fit-HD[4D] combines single-cell dosimetry (hits and dose by C-12 ions in nucleus) with molecular and cellular dynamics of individual tumor cells

(A) A tendency in decline of proliferation (i.e., number of progeny cells derived from a single mother cell) with increasing hit numbers is visible. Errorbars: SD.

(B) Representative fluorescent images of the cell cycle inhibitor p21, 53BP1, and DAPI. Cell-Fit-HD[4D] allows us to identify p21 induction in a subpopulation of cells in response to irradiation.

(C) Histogram of p21 mean intensities in single-cell nuclei , including thresholding (66 a.u.) for p21-positive cells. IR, C-12 irradiation; Ctrl, control.

(D) Mother cells with relatively high proliferative potential of ≥ 6 do not display expression of p21 in daughter cells. Dashed line, threshold for p21 positivity.

(legend continued on next page)

Architectures and workflow of Cell-Fit-HD[4D]

Cell-Fit-HD[4D] was designed to allow for standard cell culture treatment of the biological compartment irrespective of its architecture. This enables imaging of cells by standard WFM with low phototoxicity, which is identical to the imaging of ordinary multi-well plates.

The SNR in both architectures is sufficient for detection of molecular and cellular kinetics labeled by fluorescent dyes, including RIF formation, cell migration, and cell division (see STAR Methods: Signal-to-noise ratio (SNR)). The increased SNR in the mounting architecture allows us to resolve small and dim RIFs. They cannot (up to now) be robustly detected by the Trainable Weka segmentation using the wafer architecture. The large RIFs—presenting the relevant damage and of great importance for the correlation with physical beam parameters—are visible in both architectures. In addition, RIF dynamics gained from the readout signal using the wafer and the mounting architectures were similar (Figure S1E). This indicates no difference in molecular dynamics although the cells were cultured on different substrates.

We listed all parameters affecting the spatial correlation of energy deposition and cellular response in STAR Methods: Assessment of error sources in spatial correlation. The assessed mean error of ≤ 1.5 μm in the workflow (STAR Methods: Sandwich construction) is much smaller than the dimension of a cell nucleus (diameter: 10 μm).

The "initial stack" (step 1 in Figure 1C and STAR Methods: Workflow of Cell-Fit-HD[4D] using the wafer architecture) is the major factor influencing the initial number of cells to be imaged. Its recoding for a single imaging field lasts ∼30 s. This acquisition time could principally be reduced by a reduced number of imaging planes. Increasing the number of initial stacks would lengthen the time interval between irradiation and initial recording. This could be accompanied by significant cell migration and, hence, false assignment of ion traversals to cell nuclei. Despite a short time interval of ∼5 min, we did not attempt to correlate individual ion traversal with its nearest neighbor 53BP1 focus. We expect a significant risk of false correlation using a dose of 1 Gy with 27 (median) ion hits in a cell nucleus (Figure S2A). The initial stack is also crucial to account for the uncertainty in stage movement of WFM affecting spatial correlation (STAR Methods: Microscopy stage movement).

The current workflow of Cell-Fit-HD[4D] drastically increased the number of cells analyzed after irradiation compared with former designs of Cell-Fit-HD, in which only confocal readout was possible (Niklas et al., 2013c). Our biosensor abolishes the need for any kind of handling between irradiation and acquisition; the risk of contamination of the cell layer (and culture medium) is minimized, and the readout can be started immediately.

The independent readouts of both compartments expand the field of potential users of Cell-Fit-HD[4D]. WFM is a standard tool.

The readout of FNTD can be outsourced to a facility having access to confocal microscopy or the FXR700RG reader (Niklas et al., 2016). The FNTD can also be read out by WFM, decreasing the readout time by a factor of 11 (Walsh et al., 2020). The quality of the corresponding readout data and its comparison with CLSM readout data (up to now the gold standard) is subjected to current investigations.

The architecture of Cell-Fit-HD[4D], particularly the wafer architecture, shows promise for cell coating with 3D cell culture or even human biopsies in order to reflect better the *in vivo* situation of tumor treatment by IBCT. The biological compartment can principally be imaged without any fluorescent staining, i.e., by sole bright-field illumination, simplifying the modification and workflow of the biopsy. The simple and cost-effective design of our biosensor allows its usage by laboratories with limited access and expertise in detector technologies or microbeam delivery systems.

Correlation of individual molecular and cellular dynamics and deposited energy

Dose correlations based on average population numbers cannot describe a true dose-effect relationship, since the energy deposition on cellular level in IBCT is inhomogeneous (Figure 2A). Our analysis revealed a principal linear correlation between energy deposition and RIF occurrence. The substantial variation in RIF formation in response to distinct dose deposition indicates additional, e.g., molecular or cellular, parameters besides ion hits and LET (Figures 2B and S2G).

Although prominent TPs for RIF assessment are 15 min, 1 h, or 24 h post-irradiation, we found maximum representation of deposited energy by RIF in the interval 5.6 and 10.9 h (Figure 2B). This could be considered a balanced state in which the ratio of established RIFs and already repaired RIFs reaches maximum. Ongoing RIF occurrence in this interval is indicated by an increasing progression slope, whereas completed repair becomes apparent by general reduction of RIF numbers after ∼50 min (Figure S1E). In conclusion, static RIF assessment at TPs with peaking RIF numbers does not necessarily mirror received energy in a single cell. In contrast, we were able to show that dynamic RIF monitoring by determination of max RIF within 25 h increases the power as a surrogate and potential biomarker for deposited energy by ions in individual tumor cells (Figures 2C–2E) (Asaithamby and Chen, 2009). Yet, determination of max RIF at a given TP excludes already resolved RIFs. RIF tracking or summation of all emerging RIFs is not likely to improve RIF detection due to overinterpretation of signaling noise and the fact that 53BP1 foci vanish prior to mitosis (Belotserkovskaya and Jackson, 2014; Orthwein et al., 2014; Vignard et al., 2013). Quantification improvement should be feasible with stabilization of construct expression and switch to

---

(E) Three dim correlations of physical beam (hits) - molecular (p21), and cellular (proliferative potential) parameters. The plot was divided into four quadrants (I–IV) based on median hits (27) and p21 threshold. The portion of the total population is given for each quadrant. Respective analyses can help us to comprehend the radiobiological effect chain on the single-cell level and to identify potential radio-resistant subpopulations.

(F) Exemplary cell division tree of an irradiated cell demonstrates the possibility to backtrack the lineage of clonal populations and to investigate individual cell fate. Irradiation took place at time point zero.

See also Figure S3.

reporter proteins remaining on DNA damage during mitosis like MDC1 (Vignard et al., 2013).

The simplified parameter ΣLET elevated the Pearson-r coefficient for the correlation with max RIF compared with dose and is similar to the one for ion hits. This points toward a certain independence of the molecular and biological impact of single ions from the target volume, i.e., the cell nucleus being the most basic biological entity.

We performed split analysis for ion hits (irrespective of LET) and dose (irrespective of hit number). Analysis showed that the LET of a single ion in a nucleus is less indicative of resulting RIF numbers than the total number of ion hits (Figures 2D and 2E). This reflects that dose at the microscopic level can attain equal values by various combinations of hit numbers and LETs. Whereas variability in RIF-hit relationship is influenced by one physical parameter, namely LET, RIF-dose relationship is affected by ion hits and their respective LET.

Our data leave room for speculation that, within the here-applied LET range and disregarding RIF size and intensity, the probability for induction of DNA damage entity by additional ion hit is higher than for LET increase of an existing one. At equal dose, high numbers of lower-LET ions seems to create higher RIF numbers than low numbers of high-LET ions (Figure 2E). This might change for wider LET spectra and RIF integration along a single ion track in a 3D cell multilayer. Generally, Cell-Fit-HD^{4D} presents a suitable tool to further shed light on this topic (Kodaira et al., 2015; Niklas et al., 2013c).

The phenomena described in RIF formation as a response to distinct ion hits were observed on a background of immense heterogeneity and variable cellular responses. This implies a vast dependence of RIF dynamics on physical, and biological prerequisites. First, the ions' ionization pattern originates from stochastically occurring events and determines initial damage infliction and its complexity. Next, RIF formation occurs in a delayed fashion in regions of densely packed heterochromatin, and especially in cancer cells the general grade of chromatin packaging may vary substantially between subclones (Assenov et al., 2018; Mazor et al., 2016). In a similar fashion, repair capacity is highly dependent on DSB accessibility for respective proteins, an aspect that is linked to chromatin state as well as damage complexity (Goodarzi et al., 2010; Price and D'Andrea, 2013). In general, DSB repair is facilitated by a highly complex molecular machinery that is regulated on numerous levels. Therefore, repair kinetics is influenced by cell-specific levels of factors (mRNAs, proteins, micro-RNAs, signaling pathways) that regulate repair pathway activity at the TP of irradiation (Botuyan et al., 2018; Natarajan, 2016; Shibata et al., 2011). It is further known that the dynamics of DNA damage foci emergence and repair are altered with ongoing cell cycle phase due to specific regulation of repair pathways like non-homologous end-joining (G_1) and homologous repair (G_2) (Dhuppar and Mazumder, 2018; Zhao et al., 2017). Such aspects help explain the deviations from the strict hit/dose-dependent RIF formation observed in this study (Figures 2B and S2G). The future combination of Cell-Fit-HD^{4D} with additional fluorescent tags and reporters will further help decipher RIF formation in response to cell-specific energy deposition.

Although the possibility of multiple RIF forming along a single ion has been shown (Heiss et al., 2006; Niklas et al., 2013c), we did not detect a RIF for every ion track (Figures 2B and 2C). One reason could be short-lived RIFs of low 53BP1 signal not being detected by the RIF segmentation. Our verification (STAR Methods: γ-H2AX vs endogenous 53BP1) showed spatial overlap of ∼74% of γ-H2AX foci (gold standard in DSB detection) and 53BP1 foci as well as the detection of large 53BP1 foci originating from complex DSB clusters. Hence, we can exclude substantial false-negative detection of complex RIF. We cannot fully exclude the additional presence of short-lived, low-intensity RIF by imaging with 20× objective. These are usually attributed to having lesser biological relevance and are even more neglected in standard, static RIF measurements in fixed cells. Heiss et al. irradiated cells with geometrical patterns of ions but observed corresponding RIF patterns in only 61% of the cases (Heiss et al., 2006). There, C-12 ions (4.8 Mev/u, ∼290 keV/μm) with multifolds of the LETs applied in our experiments were applied. Our measured ratio is principally well in line with *in silico* simulation of RIF induction by Monte Carlo approach (Villagrasa et al., 2017). The hit/RIF ratio (∼0.2/0.22) showed great fluctuations (Figures 2B and 2C). Corresponding error bars could reflect the LET-dependence of RIF induction (Penninckx et al., 2019) by our use of ions of wide LET range. Stagnation of the slope in linear regression analysis for increasing dose values could be caused by the broad LET spectrum for corresponding increasing hit numbers (Figure S2G). Cell-Fit-HD^{4D} and microbeam technology are future tools to further shed light on this topic (Kodaira et al., 2015; McFadden et al., 2020; Zlobinskaya et al., 2012).

Since cancer cells can circumvent and downregulate cellular shutdown programs like apoptosis and senescence (Hein et al., 2014; Skinner et al., 2012), irradiation outcome may potentially vary compared with normal cells at equal microscopic energy deposition. Cell-Fit-HD^{4D} enables a decryption of the heterogeneity in the response to true dose deposition up to several days. By low cell seeding density, it should be feasible to determine the extent to which clonogenic potential within the first couple of days after irradiation correlates with formation of "classical" colonies, i.e., detection of >50 progeny cells. Our data can be interpreted as a typical scenario in which proliferative potential of cancer cells is restricted in a dose/hit-dependent manner, with single cells escaping growth arrest despite receiving great hit numbers (Figure 3E). We determined single-cell linages with low proliferative potential independent of p21, indicating alternative growth arrest induction mechanisms or asymmetric fate determination of daughter cells. Cell-Fit-HD^{4D} allows characterization of such cells in terms of morphology or active cellular programs via fluorescent reporters or endpoint staining (Figure 3B). It is also possible to trace back their lineage to test for potential asymmetric cell division with daughter cells undergoing differential fate, as we observed frequently (Figure 3F). Low-density seeding should enable post-time lapse-picking of single clonal colonies by capillaries to make them subject to further analysis like single -cell sequencing. Therefore, Cell-Fit-HD^{4D} presents a powerful tool to fully comprehend the mechanisms of ion radiation resistance in an energy-pattern-resolved manner.
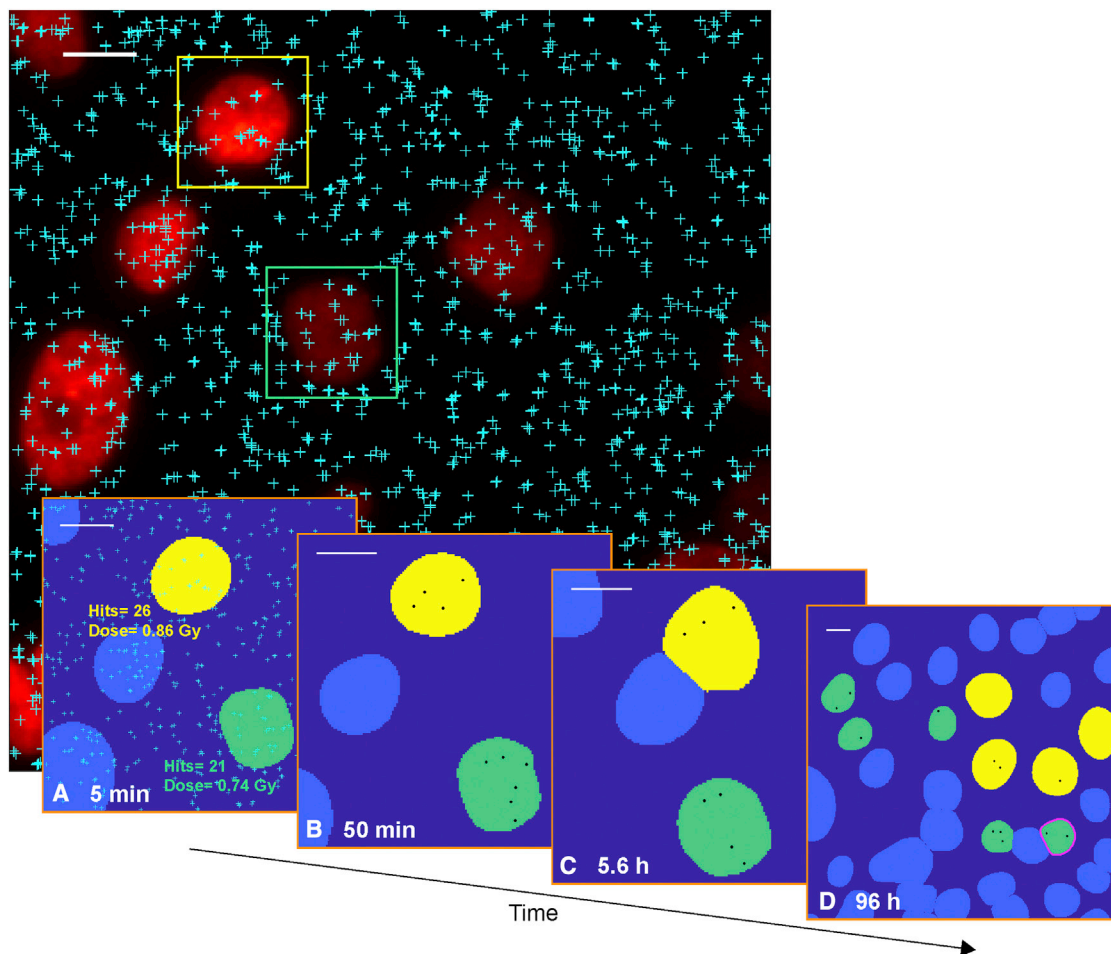
Figure 4. Cell-Fit-HD^{4D} enables correlation of physical energy deposition with time and space evolution of individual tumor cell
Fluorescent 53BP1 signal and C-12 ion hits (cyan crosses) are shown.
(A–D) Tracking of nuclei (segmented) of two mother cells: nuclei of daughter (D) and mother cells are identically colored. RIFs (black objects) and p21 status (positive cells: encircled in magenta) are displayed. Scale bars, 10 μm.

Status quo and clinical context

Cell-Fit-HD^{4D} allows translation of the microscopic energy deposition of ions into the individual cellular response, e.g., RIF formation, p21 expression, cell fate, and proliferative potential (Figures 4, 5, and S3E–S3G). It helps to address the following question: Which combination of biological cell parameters in response to which physical irradiation parameters (also dose rate using the FLASH concept) does a radiation-resistant tumor cell exhibit? In addition, our analyses identified the number of intranuclear ion hits as a good predictor for the 53BP1 RIF formation (Figure 2). The number of hits and ΣLET could be an additional parameter to a commonly used dose to quantify the cellular response on molecular and population levels. Our biosensor could provide crucial input for current mechanistic approaches to biophysical modeling of the effect of ionizing radiation to biological matter.

In the clinical context, providing multi-dimensional physical and biological information on individual tumor cells is an important step to determine which tumor entities can be effectively treated by IBCT and to understand local recurrence of a tumor after IBCT. The present treatment planning underlying physical beam parameters could be extended by a set of physical and biological (e.g., cell cycle, signaling, or immune response) parameters to maximize tumor control and minimize normal tissue complication. Target points in the cellular response cascade to ion irradiation can be detected creating multimodal (combination of IBCT with drug application) oncological concepts to maximize the benefit for the patient.

Cell-Fit-HD^{4D} is an important tool for the search of biomarkers for indirect visualization of the dose deposition. The design of Cell-Fit-HD^{4D} gives promise for cell coating with 3D cell culture or even human biopsies in order to better investigate the *in vivo* (real) response to tumor irradiation.

Limitations of study

Even if Cell-Fit-HD^{4D} is without an alternative for single-cell dosimetry in clinical ion beams, it has limitations in resolving ion beam fluences of $>10^8$ cm^{-2}. Spatial correlation of molecular

CellPress
OPEN ACCESS
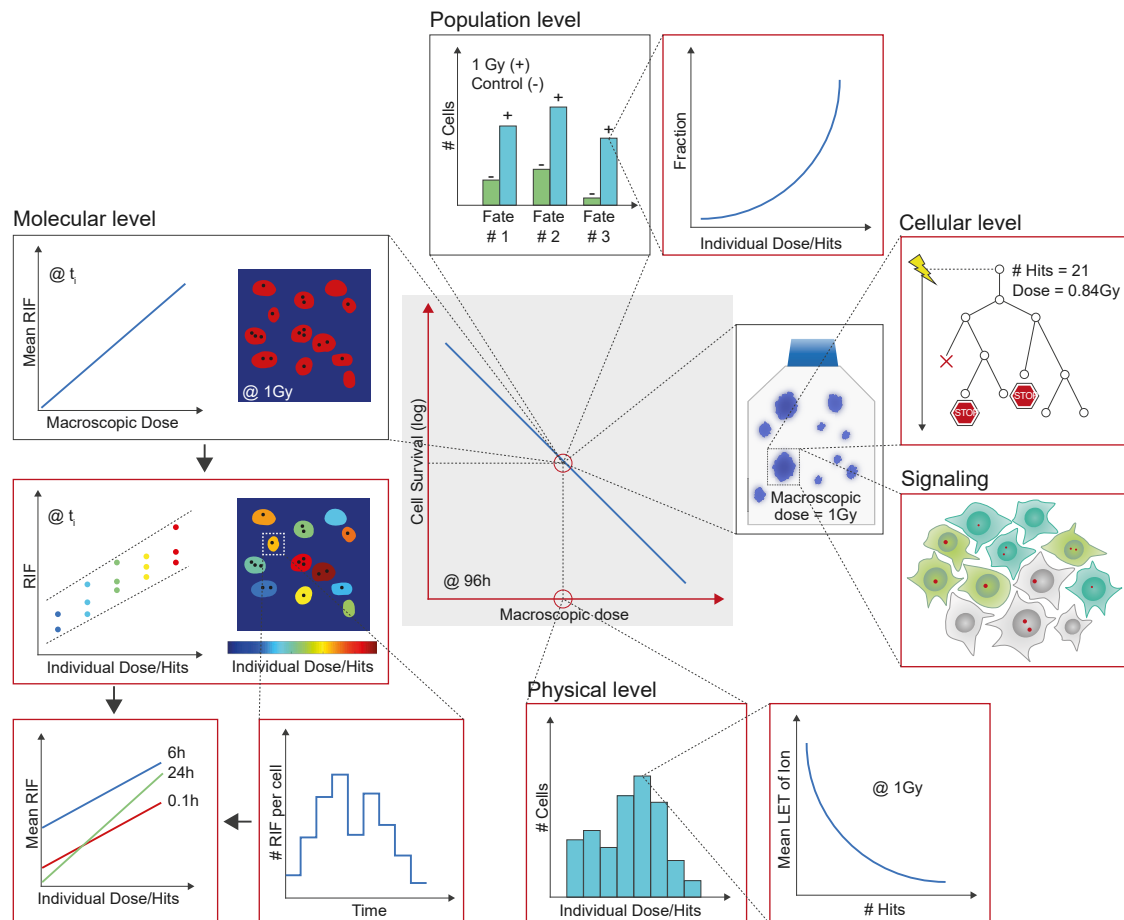
Figure 5. Schematic illustration of standard radiobiological experiment (framed in gray) and beyond, deciphered by Cell-Fit-HD4D (framed in red)

Cell survival curves (blue line) obtained by clonogenic survival assays is the current gold standard. Physical level: Unlike in standard cell culture irradiation, assigning all cells an identical dose (macroscopic dose) Cell-Fit-HD^{4D} resolves the physical energy deposition for individual cell nuclei. Molecular level: In contrast to a mean RIF value at time point t_i for a certain macroscopic dose value, Cell-Fit-HD^{4D} enables the time-dependent resolution of RIF evolution as a function of individual dose/hit deposition in a cell nucleus (color coding). Cellular/population level: In common radiobiological experiments, different cell fates are assigned to the macroscopic dose value and expressed as relative appearance. Using Cell-Fit-HD^{4D}, cell fate events can be investigated depending on the individual dose/hit deposition. Signaling: The landscape of cell biological programs can be assessed by Cell-Fit-HD^{4D} by application of fluorescent reporter constructs.

damage to single ion traversals requires low fluences (Niklas et al., 2013c). Due to cellular-as well as chromatin movement and the delay in protein complex formation around DSB, exact spatial overlap of RIF and ion track in the FNTD cannot be expected. Nearest-neighbor analysis, including fingerprint analysis, could improve spatial correlation analysis.

It is advantageous to utilize insensitive cells for Cell-Fit-HD^{4D} that are robust toward long-term imaging. Critical parameters are a.o. exposure time, acquisition intervals, and number of imaging channels and excitation wavelengths. In contrast to most tumor cell lines, more sensitive, primary cells might undergo cell death or growth arrest depending on these parameters. Cell-Fit-HD^{4D} bears the potential to study more complex subjects like tissue reactions. Important aspects are that tissue thickness could limit imaging, and movement of the tissue between irradiation and acquisition needs to be assessed.

STAR★METHODS

Detailed methods are provided in the online version of this paper and include the following:

- KEY RESOURCES TABLE
- RESOURCE AVAILABILITY
  - Lead contact
  - Materials availability
  - Data and code availability
- EXPERIMENTAL MODEL AND SUBJECT DETAILS
  - Cell culture
- METHOD DETAILS
  - Retrovirus production and transduction of A549 cells
  - Al$_2$O$_3$:C,Mg based FNTD
  - Architectures and manufacturing of Cell-Fit-HD4D
  - Irradiation of *Cell-Fit-HD^{4D}* in clinical setup

SUPPLEMENTAL INFORMATION

ACKNOWLEDGMENTS

AUTHOR CONTRIBUTIONS

M.N. and J.S. designed and developed experiments. M.N., J.S., H.L., and F.Z. performed experiments. M.N. conducted the readout of the physical compartment. J.S. performed cell culture and processing of the biological compartment. M.N., J.S., H.L., F.Z., D.W.M. W., A.A., and J.D. interpreted the data. M.N., J.S., and H.L. wrote, reviewed, and edited the manuscript. M.N, J.S, and K.R. visualized the data. S.R. and S.G. assisted in the ion track reconstruction. A.R. assisted in the development of the biosensor architecture. O.D. developed the cell tracking software and assisted in the cell tracking. T.H. supported statistical data analysis. A.A. initiated, conceptualized, and supervised the project. All authors edited the paper. All authors read and approved the final paper.

DECLARATION OF INTERESTS

The authors declare no competing interests.

REFERENCES

Akselrod, M.S., and Sykora, G.J. (2011). Fluorescent nuclear track detector technology – a new way to do passive solid state dosimetry. Radiat. Meas. *46*, 1671–1679. https://doi.org/10.1038/508133a.

Arganda-Carreras, I., Kaynig, V., Rueden, C., Eliceiri, K.W., Schindelin, J., Cardona, A., and Sebastian Seung, H. (2017). Trainable Weka Segmentation: a machine learning tool for microscopy pixel classification. Bioinformatics *33*, 2424–2426. https://doi.org/10.1093/bioinformatics/btx180.

Asaithamby, A., and Chen, D.J. (2009). Cellular responses to DNA double-strand breaks after low-dose gamma-irradiation. Nucleic Acids Res. *37*, 3912–3923. https://doi.org/10.1093/nar/gkp237.

Assenov, Y., Brocks, D., and Gerhäuser, C. (2018). Intratumor heterogeneity in epigenetic patterns. Semin. Cancer Biol. *51*, 12–21. https://doi.org/10.1016/j.semcancer.2018.01.010.

Belotserkovskaya, R., and Jackson, S.P. (2014). Keeping 53BP1 out of focus in mitosis. Cell Res. *24*, 781–782. https://doi.org/10.1038/cr.2014.62.

Belyaev, I.Y. (2010). Radiation-induced DNA repair foci: spatio-temporal aspects of formation, application for assessment of radiosensitivity and biological dosimetry. Mutat. Res. *704*, 132–141. https://doi.org/10.1016/j.mrrev.2010.01.011.

Botuyan, M.V., Cui, G., Drané, P., Oliveira, C., Detappe, A., Brault, M.E., Parnandi, N., Chaubey, S., Thompson, J.R., Bragantini, B., et al. (2018). Mechanism of 53BP1 activity regulation by RNA-binding TIRR and a designer protein. Nat. Struct. Mol. Biol. *25*, 591–600. https://doi.org/10.1038/s41594-018-0083-z.

Chan, K.F., Yum, E.H.W., Wan, C.K., Fong, W.F., and Yu, K.N. (2008). Study of DNA integrity in alpha-particle radiobiological experiments using thin CR-39 detectors. Radiat. Meas. *43*, S541–S545. https://doi.org/10.1016/j.radmeas.2008.04.043.

Dhuppar, S., and Mazumder, A. (2018). Measuring cell cycle-dependent DNA damage responses and p53 regulation on a cell-by-cell basis from image analysis. Cell Cycle *17*, 1358–1371. https://doi.org/10.1080/15384101.2018.1482136.

Dokic, I., Niklas, M., Zimmermann, F., Mairani, A., Seidel, P., Krunic, D., Jäkel, O., Debus, J., Greilich, S., and Abdollahi, A. (2015). Correlation of particle traversals with clonogenic survival using cell-fluorescent ion track hybrid detector. Front. Oncol. *5*, 275. https://doi.org/10.18632/oncotarget.10996.

Dimitrova, N., Chen, Y.C., Spector, D.L., and de Lange, T. (2008). 53BP1 promotes non-homologous end joining of telomeres by increasing chromatin mobility. Nature *456*, 524–528. https://doi.org/10.1038/nature07433.

Dokic, I., Mairani, A., Niklas, M., Zimmermann, F., Chaudhri, N., Krunic, D., Tessonnier, T., Ferrari, A., Parodi, K., Jäkel, O., et al. (2016). Next generation multi-scale biophysical characterization of high precision cancer particle radiotherapy using clinical proton, helium-, carbon- and oxygen ion beams. Oncotarget *7*, 56676–56689. https://doi.org/10.3389/fonc.2015.00275.

Dzyubachyk, O., van Cappellen, W.A., Essers, J., Niessen, W.J., and Meijering, E. (2010). Advanced Level-Set-Based Cell Tracking in Time-Lapse Fluorescence Microscopy. IEEE Trans. Med. Imaging *29*, 852–867. https://doi.org/10.1109/TMI.2009.2038693.

Eddins, S. (2013). Watershed transform question from tech support. https://blogs.mathworks.com/steve/2013/11/19/watershed-transform-question-from-tech-support/.

Friedland, W., Kundrát, P., Schmitt, E., Becker, J., Ilicic, K., Greubel, C., Reindl, J., Siebenwirth, C., Schmid, T.E., and Dollinger, G. (2019). Modeling studies on dicentrics induction after sub-micrometer focused ion beam grid irradiation. Radiat. Prot. Dosim. *183*, 40–44. https://doi.org/10.1093/rpd/ncy266.

Goodarzi, A.A., Jeggo, P., and Lobrich, M. (2010). The influence of heterochromatin on DNA double strand break repair: getting the strong, silent type to relax. DNA Repair (Amst) *9*, 1273–1282. https://doi.org/10.1016/j.dnarep.2010.09.013.

Greilich, S., Osinga, J.-M., Niklas, M., Lauer, F.M., Klimpki, G., Bestvater, F., Bartz, J.A., Akselrod, M.S., and Jäkel, O. (2013). Fluorescent nuclear track detectors as a tool for ion-beam therapy research. Radiat. Meas. *56*, 267–272. https://doi.org/10.1016/j.radmeas.2013.01.033.

Greilich, S., Jansen, J., Neuholz, A., Stadler, A., Mescher, H., and Klimpki, G. (2018). Evaluation of additional track parameters from fluorescent nuclear

track detectors to determine the LET of individual ions. Radiat. Prot. Dosim. *180*, 206–209. https://doi.org/10.1093/rpd/ncx228.

Hein, A.L., Ouellette, M.M., and Yan, Y. (2014). Radiation-induced signaling pathways that promote cancer cell survival (review). Int. J. Oncol. *45*, 1813–1819. https://doi.org/10.3892/ijo.2014.2614.

Heiss, M., Fischer, B.E., Jakob, B., Fournier, C., Becker, G., and Taucher-Scholz, G. (2006). Targeted irradiation of Mammalian cells using a heavy-ion microprobe. Radiat. Res. *165*, 231–239. https://doi.org/10.1667/rr3495.1.

Jäkel, O. (2007). State of the art in Hadron therapy. AIP Conf. Proc. *958*, 70–77. https://doi.org/10.1063/1.2825836.

Karger, C.P., and Peschke, P. (2017). RBE and related modeling in carbon-ion therapy. Phys. Med. Biol. *63*, 01TR02. https://doi.org/10.1088/1361-6560/aa9102.

Kodaira, S., Konishi, T., Kobayashi, A., Maeda, T., Ahmad, T.A.F.T., Yang, G., Akselrod, M.S., Furusawa, Y., and Uchihori, Y. (2015). Co-visualization of DNA damage and ion traversals in live mammalian cells using a fluorescent nuclear track detector. J. Radiat. Res. *56*, 360–365. https://doi.org/10.1093/jrr/rru091.

Kouwenberg, J.J.M., Ulrich, L., Jäkel, O., and Greilich, S. (2016). A 3D feature point tracking method for ion radiation. Phys. Med. Biol. *61*, 4088–4104. https://doi.org/10.1088/0031-9155/61/11/4088.

Marx, V. (2014). Cancer treatment: sharp shooters. Nature *508*, 133–138. https://doi.org/10.1038/508133a.

Mazor, T., Pankov, A., Song, J.S., and Costello, J.F. (2016). Intratumoral heterogeneity of the epigenome. Cancer Cell *29*, 440–451. https://doi.org/10.1016/j.ccell.2016.03.009.

McFadden, C.H., Rahmanian, S., Flint, D.B., Bright, S.J., Yoon, D.S., O'Brien, D.J., Asaithamby, A., Abdollahi, A., Greilich, S., and Sawakuchi, G.O. (2020). Isolation of time-dependent DNA damage induced by energetic carbon ions and their fragments using fluorescent nuclear track detectors. Med. Phys. *47*, 272–281. https://doi.org/10.1002/mp.13897.

Natarajan, V. (2016). Regulation of DNA repair by non-coding miRNAs. Non-coding RNA Res. *1*, 64–68. https://doi.org/10.1016/j.ncrna.2016.10.002.

Niklas, M., Bartz, J.A., Akselrod, M.S., Abollahi, A., Jäkel, O., and Greilich, S. (2013a). Ion track reconstruction in 3D using alumina-based fluorescent nuclear track detectors. Phys. Med. Biol. *58*, N251–N266. https://doi.org/10.1088/0031-9155/58/18/N251.

Niklas, M., Abdollahi, A., Akselrod, M.S., Debus, J., Jäkel, O., and Greilich, S. (2013b). Subcellular spatial correlation of particle traversal and biological response in clinical ion beams. Int. J. Radiat. Oncol. Biol. Phys. *87*, 1141–1147. https://doi.org/10.1016/j.ijrobp.2013.08.043.

Niklas, M., Greilich, S., Melzig, C., Akselrod, M.S., Debus, J., Jäkel, O., and Abdollahi, A. (2013c). Engineering cell-fluorescent ion track hybrid detectors. Radiat. Oncol. *8*, 141. https://doi.org/10.1186/1748-717X-8-141.

Niklas, M., Zimmermann, F., Schlegel, J., Schwager, C., Debus, J., Jäkel, O., Abdollahi, A., and Greilich, S. (2016). Registration procedure for spatial correlation of physical energy deposition of particle irradiation and cellular response utilizing cell-fluorescent ion track hybrid detectors. Phys. Med. Biol. *61*, N441–N460. https://doi.org/10.1088/0031-9155/61/17/N441.

Niklas, M., Henrich, M., Jäkel, O., Engelhardt, J., Abdollahi, A., and Greilich, S. (2017). STED microscopy visualizes energy deposition of single ions in a solid-state detector beyond diffraction limit. Phys. Med. Biol. *62*, N180–N190. https://doi.org/10.1088/1361-6560/aa5edc.

Okayasu, R. (2012). Repair of DNA damage induced by accelerated heavy ions—a mini review. Int. J. Cancer *130*, 991–1000. https://doi.org/10.1002/ijc.26445.

Orthwein, A., Fradet-Turcotte, A., Noordermeer, S.M., Canny, M.D., Brun, C.M., Strecker, J., Escribano-Diaz, C., and Durocher, D. (2014). Mitosis inhibits DNA double-strand break repair to guard against telomere fusions. Science *344*, 189–193. https://doi.org/10.1126/science.1248024.

Osinga, J.-M., Akselrod, M.S., Herrmann, R., Hable, V., Dollinger, G., Jäkel, O., and Greilich, S. (2013). High-accuracy fluence determination in ion beams using fluorescent nuclear track detectors. Radiat. Meas. *56*, 294–298. https://doi.org/10.1016/j.radmeas.2013.01.035.

Penninckx, S., Cekanaviciute, E., Degorre, C., Guiet, E., Viger, L., Lucas, S., and Costes, S.V. (2019). Dose, LET and strain dependence of radiation-induced 53BP1 foci in 15 mouse strains ex vivo introducing novel DNA damage metrics. Radiat. Res. *192*, 1–12. https://doi.org/10.1667/RR15338.1.

Price, B.D., and D'Andrea, A.D. (2013). Chromatin remodeling at DNA double-strand breaks. Cell *152*, 1344–1354. https://doi.org/10.1016/j.cell.2013.02.011.

Rahmanian, S., Niklas, M., Abdollahi, A., Jäkel, O., and Greilich, S. (2017). Application of fluorescent nuclear track detectors for cellular dosimetry. Phys. Med. Biol. *62*, N2719–N2740. https://doi.org/10.1088/1361-6560/aa56b4.

RStudio Team (2015). RStudio: Integrated Development Environment for R, Boston, MA (RStudio). http://www.rstudio.com/.

Schardt, D., Elsässer, T., and Schulz-Ertner, D. (2010). Heavy-ion tumor therapy: physical and radiobiological benefits. Rev. Mod. Phys. *82*, 383–425. https://doi.org/10.1103/RevModPhys.82.383.

Schneider, C.A., Rasband, W.S., and Eliceiri, K.W. (2012). NIH image to ImageJ: 25 years of image analysis. Nat. Methods *9*, 671–675. https://doi.org/10.1038/nmeth.2089.

Shibata, A., Conrad, S., Birraux, J., Geuting, V., Barton, O., Ismail, A., Kakarougkas, A., Meek, K., Taucher-Scholz, G., Löbrich, M., et al. (2011). Factors determining DNA double-strand break repair pathway choice in G2 phase. EMBO J. *30*, 1079–1092. https://doi.org/10.1038/emboj.2011.27.

Siddiqui, M.S., François, M., Fenech, M.F., and Leifert, W.R. (2015). Persistent γH2AX: a promising molecular marker of DNA damage and aging. Mutat. Res. Rev. Mutat. Res. *766*, 1–19. https://doi.org/10.1016/j.mrrev.2015.07.001.

Skinner, H.D., Sandulache, V.C., Ow, T.J., Meyn, R.E., Yordy, J.S., Beadle, B.M., Fitzgerald, A.L., Giri, U., Ang, K.K., and Myers, J.N. (2012). TP53 disruptive mutations lead to head and neck cancer treatment failure through inhibition of radiation-induced senescence. Clin. Cancer Res. *18*, 290–300. https://doi.org/10.1158/1078-0432.CCR-11-2260.

Sykora, G.J., Akselrod, M.S., Benton, E.R., and Yasuda, N. (2008). Spectroscopic properties of novel fluorescent nuclear track detectors for high and low LET charged particles. Radiat. Meas. *43*, 422–426. https://doi.org/10.1016/j.radmeas.2007.11.009.

Vignard, J., Mirey, G., and Salles, B. (2013). Ionizing-radiation induced DNA double-strand breaks: a direct and indirect lighting up. Radiother. Oncol. *108*, 362–369. https://doi.org/10.1016/j.radonc.2013.06.013.

Villagrasa, C., Meylan, S., Gonon, G., Gruel, G., Giesen, U., Bueno, M., and Rabus, H. (2017). Geant4-DNA simulation of DNA damage caused by direct and indirect radiation effects and comparison with biological data. EPJ Web. Conferences *153*, 04019. https://doi.org/10.1051/epjconf/201715304019.

Walsh, D.W.M., Liew, H., Schlegel, J., Mairani, A., Abdollahi, A., and Niklas, M. (2020). Carbon ion dosimetry on a fluorescent nuclear track detector using widefield microscopy. Phys. Med. Biol. *65*, 21NT02. https://doi.org/10.1088/1361-6560/abb7c5.

Zhao, X., Wei, C., Li, J., Xing, P., Li, J., Zheng, S., and Chen, X. (2017). Cell cycle-dependent control of homologous recombination. Acta Biochim. Biophys. Sin (Shanghai) *49*, 655–668. https://doi.org/10.1093/abbs/gmx055.

Zlobinskaya, O., Dollinger, G., Michalski, D., Hable, V., Greubel, C., Du, G., Multhoff, G., Röper, B., Molls, M., and Schmid, T.E. (2012). Induction and repair of DNA double-strand breaks assessed by gamma-H2AX foci after irradiation with pulsed or continuous proton beams. Radiat. Environ. Biophys. *51*, 23–32. https://doi.org/10.1007/s00411-011-0398-1.

STAR★METHODS

KEY RESOURCES TABLE

REAGENT or RESOURCE	SOURCE	IDENTIFIER
Antibodies		
Mouse p21 Waf1/Cip1/CDKN1A (F-5)	*Santa Cruz*	*Cat#sc-6246; RRID: AB_628073*
Rabbit p53 binding protein 1 (53BP1)	*Cell Signaling Technology*	*Cat#4937; RRID: AB_10694558*
Mouse Anti-Phospho-Histone H2A.X (Ser 139)	*Cell Biolabs*	*Cat#STA-321*
Bacterial and virus strains		
Retro-X Universal Packaging System	*Takara*	*Cat# 631530*
Chemicals, peptides, and recombinant proteins		
Dulbecco's phosphate buffer saline (DPBS)	PAN Biotech	Cat# P04-53500
Dulbecco's Modified Eagle Medium (DMEM)	Merck Millipore	Cat#FG0415
DMEM Phenol red-free	Merck Millipore	Cat#F0475
Heat Inactivated Fetal Bovine Serum (FBS)	Merck Millipore	Cat# #S0615
Penicillin/Streptomycin	Thermo Fisher	Cat# 15140
Experimental models: Cell lines		
Human: A549 lung carcinoma cells	ATCC	Cat#CCL-185; RRID:CVCL_0023
Recombinant DNA		
Apple-53BP1trunc	Addgene	Plasmid #69531
Software and algorithms		
ImageJ	Schneider et al. (2012)	https://imagej.nih.gov/ij/
MatLab	MathWorks	https://de.mathworks.com/products/matlab.html
Level-set based CellTracker	Dzyubachyk et al., 2010	DOI: 10.1109/TMI.2009.2038693
RStudio	RStudio Team	https://www.rstudio.com/products/rstudio/
Code applied for data generation reported here	*This paper*	DOI: 10.17632/cdt269pw7 m.1
Other		
Fluorescent Nuclear Track Detector (FNTD)	Landauer Inc	

RESOURCE AVAILABILITY

Lead contact
Further information and requests for resources and reagents should be directed to and will be fulfilled by the Lead Contact Dr. Julian Schlegel (j.schlegel@dkfz.de).

Materials availability
All materials and constructs used in this study are maintained by Prof. Dr. Dr. Abdollahi's laboratory and are available upon request.
This study did not generate new unique reagents.
There are restrictions to the availability of FNTDs due to commercial distribution by the manufacturer.

Data and code availability
- All data reported in this paper will be shared by the lead contact upon request.
- All fundamental code applied for data generation reported in this paper is available online (https://doi.org/10.17632/cdt269pw7m.1). Additionally requested code will be shared by the lead contact upon request.
- Any additional information required to reanalyze the data reported in this paper is available from the lead contact upon request.

EXPERIMENTAL MODEL AND SUBJECT DETAILS

Cell culture

A549 human Non-Small-Cell-Lung-Carcinoma (NSCLC) cells (ATTC CCL-185) were cultured using Dulbecco's Modified Eagle's Medium (DMEM) supplied with 10% Fetal Bovine Serum (FBS) and 1% Penicillin/Streptomycin at 37 °C, 5% CO_2. For live-cell imaging, respective medium lacking phenol-red was used.

METHOD DETAILS

Retrovirus production and transduction of A549 cells

A549 cells were retrovirally transduced with a construct coding for the N terminus of 53BP1 fused to the sequence coding for fluorescent mCherry-protein (Addgene Catalog # 19835; originally described in (Dimitrova et al., 2008). Retroviral particles carrying the 53BP1-mCherry plasmid were generated via transfection of HEK293 stably expressing gag/pol proteins with VSV-G-plasmid and the transfer plasmid according to standard method. Retrovirus-containing supernatants were taken and applied on A549 cell without further concentration. Selection occurred with puromycin (5 μg/mL). Puromycin-selection was applied on a regular base during culturing as well as during the experimental course.

Al_2O_3:C,Mg based FNTD

The fluorescent nuclear track detector (FNTD) is a detector for single ion track visualization with sub-μm resolution. A detailed description of the FNTD can be found in (Akselrod and Sykora, 2011; Greilich et al., 2013). The FNTD is usually read out by confocal laser scanning microscopy (CLSM). Optical Nanoscopy, i.e. STED microscopy, provides resolution beyond diffraction limit (Niklas et al., 2017). The FNTD was in the shape of a wafer of thickness 100 μm and of diameter 20 mm and is made of aluminum oxide doped with carbon and magnesium ions (Al_2O_3:C,Mg). The crystal structure exhibit F_2^{2+}(2Mg)-centers fluorescent color centers. They undergo transformation when capturing secondary electrons released by traversing ions. This leads to a unique footprint of the traversing ions in the FNTD. The transformed color centers can be excited at 620 nm, prompting fast fluorescence at 750 nm. The FNTD is sensitive for ions with LET >0.5 keV/μm (Osinga et al., 2013; Sykora et al., 2008). The detection efficiency is close to 100% for the ion spectra found in IBCT (Osinga et al., 2013).

Architectures and manufacturing of Cell-Fit-HD4D

We engineered two different architectures for *Cell-Fit-HD^{4D}*:

- *wafer architecture* and
- *mounting architecture.*

Cell viability, Signal-to-Noise Ratio (SNR), RIF frequency and the feasibility of precise extrapolation of ion tracks into cell layer were validated. Corresponding information is given below. Information on validation of track extrapolation is given in the paragraph sandwich construction below.

Wafer architecture

We substituted the glass bottom of a conventional 6-well imaging plate with a fluorescent nuclear track detector (FNTD, see above) in the shape of a wafer and seeded cells on top, as for usual cell culture experiments. In this design of the biosensor the cell layer forming the biological compartment is directly adherent to the FNTD forming the physical compartment.

For the manufacturing approach, we cleaned the surfaces of the imaging plate with ethanol (70%) to disinfect them and to prevent interfering particles. Small droplets of histo-acryl glue (B. Braun GmbH, Art. Nr. 9381104) - in total 8 μL - were placed on the circular-shaped frame of the bottom of the well bottom. We found that this applied volume minimizes the chance of contamination of the inner well with histo-acryl, while ensuring solid and enduring stability. The sterilized wafer (FNTD) was gently pressed by means of a suction device onto this circular frame (adhesive surface). The number and position of the wells to be modified by FNTD wafer depends on the experimental setup. Distance between irradiated and control samples is recommended to simplify the irradiation setup in terms of shielding the controls from the ion beam.

We found that upside-down placement of the modified imaging plate in a conventional cell culture incubator (37 °C; 5% CO_2, humidity) for approx. one minute is sufficient to allow complete polymerization of histo-acryl. Since potential glue residues could occasionally be detected, both surfaces of the wafer were cleaned by help of a cotton bud ear stick soaked in ethanol (70%). This further reduced the probability of later detection of microscopic glue residues in the cell medium. Quality control of the cleaned wafer surfaces was performed by conventional bright-field microscopy (magnification: 20×). To ensure clearance from any chemical or biological remains, we additionally sterilized and washed the modified wells with 1 mL ethanol, followed by 2 × 1 mL PBS. Robust fluid retention was confirmed by incubation of the multiwell plate filled with cell medium in the incubator for approx. 30 min. We noticed that this test incubation needed to occur at experimental conditions (37 °C; 5% CO_2, humidity), as temperature and humidity could influence glue stability.

Approx. 18 h before irradiation A549 cells were seeded on top of the wafer using DMEM. The general biocompatibility of the FNTD to allow for adherent cell layers was demonstrated in (Dokic et al., 2015; Niklas et al., 2013a). We experimentally determined 150,000

cells/well as a good seeding number which provides sufficient number of cells per imaging field while allowing for population expansion over the course of several days. Of course, the cell seeding density and hence the number of cells to be imaged can principally be adapted according to the aim of the experiment. We further noticed that, for optimally uniform cell distribution, incubation at room temperature for approx. 20 min is helpful to allow cells to settle down without influence of hydrodynamics. The biosensor was then stored in the incubator overnight to allow for cell adherence. Cells were subsequently monitored by microscopy to ensure attachment on the modified well bottom and normal physiological morphology. Unusual morphology or floating cells were traced back to contact of glue residues with the medium.

Mounting architecture

The rationale behind the mounting architecture is the spatial separation of the physical from the biological compartment minimizing the interference of the readouts of both compartments. A recording of fluorescent dyes in the cell layer by widefield microscopy (WFM) with excitation wavelength close to 405 nm would considerably alter the signal of the track spots in the FNTD wafer. Also, a read-out of the biological compartment using an excitation wavelength close to 620 nm would principally interfere with the emission signal of the wafer at the border region between wafer and cell layer. Additionally, the advantage of the mounting architecture in comparison to the wafer architecture is the possibility to directly transfer experience in culturing different cell lines on ordinary imaging plates.

In the mounting architecture the cells are cultured on the glass bottom of a single well of a 12-well-glass bottom dish. The well was covered with a lid made of glass which has a carrier with the FNTD fixed on its bottom. Since the lid gets removed during the long-term read-out of the cell layer, the FNTD could be read-out in parallel and independently by CLSM. Glass was chosen for the carrier of the mounting architecture to minimize potential displacement between cell layer and FNTD caused by thermal expansion during the time interval between irradiation and initial read-out. We identified the displacement in this critical time span to be less than 1 μm. Detailed information on the experiment for defining the displacement can be found in the paragraph *Thermal Expansion of the Glue* below. On the contrary, the displacement was in the order of several μm using a lid made of plastic. The principal reason behind was absorption of the cell culture medium by the plastic.

Thermal expansion of the glue

We investigated the influence of the glue used in assembling of the mounting architecture on spatial correlation of the information of the biological and physical compartment. In particular, we investigated, whether dilatation of the glue based on temperature change during the irradiation of Cell-Fit-HD[4D] could influence the ion track reconstruction in the cell layer. For the validation experiment the glass bottom in the mounting architecture was replaced by a wafer. We principally tested histo-acryl glue (B. Braun GmbH, Cat-No. 9381104) and *Sekundenkleber Blitzschnell Präzision* (UHU).

We mimicked the assembling, irradiation, and read-out procedure of *Cell-Fit-HD[4D]*: We assembled the mounting architecture and incubated the multiwell plate filled with culture medium (without cell layer) in the incubator (humified atmosphere) for approx. 24 h (step 1). After replacing the culture medium and sealing the multiwell plate with *Parafilm* under room temperature (RT, step 2) we stored the plate again in the incubator for 6 min (step 3). We simulated the irradiation by placing the biosensor in an upright position for 6 min under RT (step 4). We stored the biosensor for additional 2 min at RT to account for the transfer from the irradiation facility to the microscope (step 5). In the last step, we ran the initial read-out of the biosensor at 37 °C (step 5). At the end of steps 2-5, we performed imaging of the *spinels* located in the wafer and in the FNTD by WFM. For steps 2-5 we defined five control point pairs (*cpps*) using the recorded *spinels* in the wafer and in the FNTD. We calculated the distance in the horizontal plane for each *cpp* for each image acquisition to detect any spatial shift during the temperature change caused by the changing viscosity of the glue. We identified the shift in the critical time span between irradiation and initial read-out to be less than 1 μm.

Cell viability

We investigated whether the cell viability using the *wafer*-differs from the cell viability using the mounting architecture. Cell number dynamics was recorded for each imaging field (Figure S1C). For this purpose, a binary mask was created by *global thresholding* using the recorded fluorescent signal of 53BP1 and modified by the functions *dilation* and *erosion* in *Matlab*. To separate individual cell nuclei *watershed segmentation* was used as presented in (Eddins, 2013). This algorithm turned out to be more sensitive in detection of nuclei with low 53BP1 expression compared to *LSetCellTracker*.

Signal-to-noise ratio (SNR).

We investigated the signal-to-noise ratio (SNR) in the live-cell imaging using the mounting architecture and the *wafer architecture*. The SNR in both architectures is sufficient for detection of molecular and cellular kinetics labelled by fluorescent dyes including RIF formation, cell migration and cell division. There is a great inter-cellular variation in the signal of the recorded cell nuclei. This is based on the substantial variation of 53BP1 expression within the cell population. The cell nuclei cultured on the wafer principally appeared to be dimmer in the imaging data compared to the nuclei cultured on the glass bottom in the mounting architecture. The edges (gradient) of the foreground object in the mounting architecture appeared to be steeper compared to the *wafer architecture*. The SNR gained in both designs was however sufficient to perform nucleus segmentation and cell tracking using the *Matlab* routine *LSetCellTracker* and RIF detection using *Trainable Weka segmentation* plugin for *ImageJ* (Arganda-Carreras et al., 2017; Schneider et al., 2012). It was not always possible for the segmentation routine (*LSetCellTracker*) to identify the correct edges of the nuclei. The resulting areas sometimes appear too large or too small. Yet, this observation is rather subjective as there is no explicit definition of the "correct" edges of the nuclei. We, therefore, used identical segmentation parameters for the *mounting-* and *wafer architecture* to get consistent and comparable results.

RIF segmentation and frequency

The RIFs (53BP1 foci) emerging after irradiation were segmented by *Trainable Weka segmentation* plugin for *ImageJ* (Arganda-Carreras et al., 2017). Input data were gained after nucleus segmentation and cell tracking using the *LSetCellTracker* code written in *Matlab.*

We investigated whether the extracted RIF (53BP1) dynamics gained from the read-out signal of *wafer-* and the mounting architecture of *Cell-Fit-HD^{4D}* were similar. With this test, we were looking for hints indicating different molecular dynamics since the cells were cultured on different substrates (glass vs aluminum oxide). As depicted in Figure S1A, cells cultured on aluminum oxide (*wafer-*) or glass (mounting architecture) and being exposed to 0.5 Gy (C-12) showed similar RIF dynamics. The mean number of RIFs in a nucleus peaked at approx. 50 min post irradiation, followed by a decline. Cells cultured on wafer and being exposed to 1 Gy (C-12) exhibit principally similar RIF dynamics with a delayed maximum at approx. 67 min after irradiation. The maximum mean RIF numbers are shifted towards greater values by a factor of approx. 2.01 when comparing the data set from 0.5 Gy and 1 Gy wafer. The shift is - as expected - caused by the higher dose deposition in the 1 Gy experiment. The difference in peak values by a factor of approx. 1.4 when comparing the 0.5 Gy *wafer-* and 0.5 Gy mounting architecture datasets is most likely caused by the decreased SNR in the *wafer architecture*. To principally account for the difference in SNR, the *Trainable Weka Segmentation* tool was trained for the *wafer-* and the mounting architecture datasets individually.

Sandwich construction

The ions are principally traveling on straight lines when traversing the biosensor. We still performed a validation experiment to prove the accuracy in ion track reconstruction using the read-out signals of the FNTD in the mounting architecture (Figure S1D). For this purpose, we substituted the glass bottom in the mounting architecture with a FNTD in the form of a thin wafer (Figure S1F). The distance between FNTD and wafer (Δh) was approx. 45 μm. We performed C-12 ion irradiation using the identical irradiation plan without stopping material. We reconstructed the ion trajectories both in the wafer (blue arrows) and in the FNTD (red arrows) using the ion track reconstruction routines. Additionally, we extrapolated the ion trajectories from the FNTD onto the wafer surface and tested the spatial overlap of their coordinates with the coordinates of the ion trajectories reconstructed in the wafer.

Since we were using the identical read-out protocol as for live-cell imaging we performed initial read-out of the wafer and of the FNTD by WFM within a single step. The *mountingarchitecture* was then disassembled and the wafer and FNTD were scanned independently by CLSM. A tile scan and subsequent stitching routine was performed only for the read-out of the wafer. Both recorded confocal image stacks were registered with the data set recorded in the initial read-out. The associated ion trajectories (originating from the FNTD and from the wafer) were identified and linked using the nearest neighbor algorithm in *Matlab*. This pairing was validated manually. We tested spatial overlap of the reconstructed ion trajectories within two regions with a mean displacement of 1.02 and 1.30 μm, respectively. These values are much smaller than the dimension of a single cell nucleus. In general, we overestimated this error since we performed image registration twice (see workflow below). In addition, we also neglected possible expansion of the glue resulting in a lateral displacement of wafer and FNTD and we were conducting the experiments at room temperature.

Due to the industrial manufacturing of the glass bottom multiwell dishes (*MaTek*) with limited precision, the distance Δh between glass bottom and FNTD varies. This, in principle, does not disturb the ion track reconstruction, but is reflected in greater prediction intervals (PIs) (Niklas et al., 2013b).

Irradiation of *Cell-Fit-HD^{4D}* in clinical setup

Irradiation of *Cell-Fit-HD^{4D}* was performed at Heidelberg Ion Beam Therapy Center (HIT) at Heidelberg University Hospital, Germany. The biosensor was aligned perpendicular to the incident carbon ion beam (Figure 1B). Irradiation plan was similar to (Dokic et al., 2016). The cell layer was positioned in the middle of a 1 cm wide spread-out Bragg peak (SOBP). The water equivalent depth was approx. 3.5 cm. Planned physical doses were 1 Gy and 0.5 Gy, respectively. Both irradiations were principally identical except for rescaling of the ion beam fluence to gain defined physical dose. With the ion beam fluence used here, non-resolvable overlaps of ion tracks should not occur based on Monte Carlo simulation but need to be expected with increasing fluence. PMMA (thickness of 3 cm) was used as blocking material in front of the biosensor. It acts as healthy tissue equivalence in front of the tumor. Tumor cells in the wells 1 and 4 (Figures S1A and S1B) were facing the ion beam. For the control additional PMMA block (thickness of 21 cm) was placed in front of the wells 3 and 6.

To ensure no leakage of the culture medium during irradiation, it proved effective to seal the wells with Parafilm (Pechiney Plastic Packaging Inc., USA, Cat. No. PM996) and apply slight pressure by a sheet of a wiping paper under the plate lid. This construction was maintained stable by additional wrapping of the multiwell plate sides with Parafilm.

Workflow of *Cell-Fit-HD^{4D}* using the *wafer architecture*

The workflow for the *wafer-* and for the the mounting architecture are similar. Specific information on the latter workflow is given in the paragraph workflow of mounting architecture below. Prior to irradiation we replaced the conventional DMEM cell medium with pre-warmed phenol-free DMEM as this decreased background signals during imaging. Immediately after ion irradiation, *Cell-Fit-HD^{4D}* was transferred to the temperature-controlled (37 °C, 5% CO_2) widefield microscope and the Parafilm used under irradiation was removed. To guarantee a minimum delay between irradiation and acquisition start, all parameters for the microscope read-out (using *ScanR, Olympus*) were set in advance.

In an initial read-out, the so-called *initial stack*, the FNTD and the tumor cells were scanned in a single step (Step 1, Figure 1C). Thus, the initial position of the tumor cells (fluorescent signal) as well as the *spinels* in the wafer (transmitted light), acting as landmarks for later image registration, were recorded. The *spinels* and the initial positions of the tumor cells are crucial to enable precise spatial correlation of physical energy deposition and cellular response directly after irradiation.

In a second step the live-cell imaging of the biological compartment was performed up to five days by WFM (Step 2, Figure 1C). Typical acquisition interval Δt was 45 min to probe the cellular and molecular dynamics. A sequence of shorter time intervals of 15 min – in total 2 h - was added at the start of the imaging process to probe the early dynamics of 53BP1 after irradiation. The interval Δt can principally be varied. We applied the combination of Δt = 15 min (first 9 time points, TP) and Δt = 45 *min* to record the early DNA damage repair but also to avoid phototoxicity by the widefield imaging at later TPs. A sole recording of the cell layer by bright field microscopy without fluorescence imaging could further decrease phototoxicity

After live cell monitoring (i.e. at the TP of interest), the *Cell-Fit-HD⁴ᴰ* was transferred to a CLSM to read out the FNTD (Step 3, Figure 1C). In this step the fluorescent track spots, i.e. unique foot prints of the traversing ions left in the FNTD, and the *spinels* were recorded sequentially. Both read outs (together with stitching and image registration routines) were needed to allow reconstruction of each ion track (red arrows) into the cell layer recorded in the initial read-out with sub-μm precision.

After completion of the experiment, the biosensor could be dissembled and the FNTD could be reused after bleaching.

Workflow of *Cell-Fit-HD⁴ᴰ* using the mounting architecture

The insert of the well (containing the cells and the FNTD) was filled with culture medium prior to irradiation. For this purpose, the lid of the mounting architecture contains small apertures. To ensure optimal cell physiological conditions during live-cell imaging, the lid including the FNTD gets removed after the initial read-out (Step 1 in Figure 1C). For the removal, force is applied gently at the adhesive joints (labelled in yellow in Figure S1D) by a pair of tweezers. The FNTD is then scanned independently by CLSM.

Read-out of *Cell-Fit-HD⁴ᴰ*

The read out is principally similar for both architectures of *Cell-Fit-HD⁴ᴰ*. Except for the initial read-out, the physical compartment (FNTD) and the biological compartment (cell layer) are recorded independently.

The physical compartment was imaged by the CLSM LSM710 ConfoCor3 (Carl-Zeiss AG). A detailed readout protocol is presented in (Greilich et al., 2013; Niklas et al., 2016). Briefly, tile scans consisting of overlapping imaging stacks were recorded: 40x oil objective, zoom = 1.1, number of rescans (line sum) = 2, dwell time = 6.3 μs. An imaging stack consists of 21 imaging planes of dimensions 1024 × 124 pixels (1 pixel = $0.189 \times 0.189 um^2$) separated by 5 μm (without correction for refractive index mismatch) in axial (z) direction (Niklas et al., 2013b). Transmission photomultiplier tubes (T-PMTs) were used to record the *spinels* in the transmitted-light channel; avalanche photo diodes (APDs) with long-pass filter (detection window >650 nm) were used to record the physical track information (i.e. track spots) in the fluorescence channel in parallel. The *spinels* are crystal defects in the FNTD employed as landmarks for subsequent image registration (see paragraph Stitching and registration procedure below). Imaging started 5 μm below the FNTD surface.

The biological compartment was recorded by inverted WFM (IX83, Olympus), including 20×/NA 0.8 air objective, illumination system Lumencore spectra X LED system, Hamamatsu Orca flash V2 sCMOS camera (exposure time = 4 ms and 200 ms for brightfield and fluorescence channel, respectively), filter-set, and an incubation chamber (humidified atmosphere, standard culture conditions: 37°C, 5% CO2). Image stacks at several positions were recorded. A stacks contained 3 planes of dimensions 2048 × 2048 pixels ($665.6 \times 665.6 \ \mu m^2$, pixel size of $0.325 \times 0.325 \ \mu m^2$) separated by 1.5 μm (without correction for refractive index mismatch). The vertical position of the cell layer was detected by an autofocus routine. For subsequent image analysis maximum intensity z projections of the recorded image stacks of the cell layer were created.

In the initial read-out (Figure 1C) the physical and biological compartment were scanned sequentially in a single step by WFM to record the *spinels* (FNTD) and biological information (i.e. cell layer). The scan comprised imaging stacks of several positions. Each stack was covering the total FNTD and the cell layer in vertical dimension (2048 × 2048 pixels, $665.6 \times 665.6 \ \mu m^2$, pixel size of $0.325 \times 0.325 \ \mu m^2$) separated in z by 5 μm (without correction for refractive index mismatch).

Concerning the read-out of the mounting architecture, the FNTD was mounted in a glass bottom dish (MatTek Corporation, 6 well, Part No. P06G-1.5-20-F) and was recorded as described above.

Stitching and registration procedure

A detailed description of the stitching and registration procedure can be found in (Niklas et al., 2016). A single imaging field recorded by the WFM (20× objective) comprised 4 × 4 tiles recorded by CLSM (40× objective). The zoom was set to 1.1 to decrease vignetting effects at the imaging margin. For image processing purposes the single tiles comprising an imaging stack of 20 layers were normalized using the in-house written software called *FNTD package* (Kouwenberg et al., 2016). All tiles were recorded with a spatial overlap of approx. 20 × 193.5 μm². A binary mask was computed comprising the segmented track spots as foreground objects of the maximum intensity projection of each imaging stack (using 16 imaging planes). To create a binary mask a sequence of thresholding (threshold value of 0.2 of the normalized data), filling of regions and holes and replacement of small objects (≤ 4 pixel) was applied to the raw data. The segmented track spots are acting as unique fingerprints for the subsequent stitching process. In a first step all neighboring tiles of the 4 × 4 scan were stitched. Using the stitching parameters, a complete row (comprising 4 tiles) was reconstructed. Each row was cropped at its upper imaging margin (approx. 9 μm) to erase areas with zero intensity introduced by

the stitching. In a second step all neighboring rows were stitched. Finally, the imaging field was reconstructed using the stitching parameters of the neighboring rows. The accuracy of stitching is directly reflected in the subsequent image registration process. For additional quality control an overlap of the stitched tiles was visualized in red-green color coding. The spatial overlap was thus visualized in yellow.

For the registration of the confocal and widefield imaging data the *spinels* recorded in the transmission light channel were used as landmarks. The intensity-weighted centroid of each *spinel* was computed in the maximum intensity projection of the confocal (input) and widefield (base) imaging stacks which were initially stitched. For the registration process a projective transformation was used. All *spinels* detected were used as landmarks. To control accuracy of transformation the Euclidean distance between the *spinels* in the input and base image acting as control point pairs (*cpps*) as well as the four corner angles of the registered confocal imaging field were calculated. The mean distance between *cpps* was on average less than 0.4 μm for all imaging fields registered. The corner angles of the registered imaging fields were in the range of $90° \pm 0.3°$.

Post-time lapse imaging staining and image processing

Following live-cell imaging, culture medium was immediately aspirated and cells were washed with PBS, followed by fixation with ice-cold 70% EtOH and storage at $-20\,°$C for a minimum of 24 h. For protein staining, cells were washed with PBS, and concomitant blocking and cell permeabilization was conducted with 3% BSA, 0.2% Triton X-100 in PBS for 20 min. Primary antibodies (mouse anti-γH2AX, Cell Biolabs, STA-321, 1:100; rabbit anti-53BP1, Cell Signaling Technology, 4937S, 1:200; mouse anti-p21, Santa-Cruz, sc-6246, 1:50) were diluted in washing buffer (0.6% BSA, 0.02% TritonX-100 in PBS) and applied on top of FNTD for overnight incubation at 4 °C. Wells were consecutively washed two times for 5 min in washing buffer before incubation with secondary antibodies (Alexa Fluor-488 goat anti-mouse IgG, Invitrogen, A-11029; Alexa Fluor-647 goat anti-mouse IgG, Invitrogen, A-21236, Alexa Fluor-488 donkey anti-rabbit IgG, Invitrogen, A-21206; all 1:400) for 5 h at 4 °C. Cells were washed sequentially with washing buffer and PBS for 5 min each and stored in fresh PBS at 4 °C until microscopic acquisition.

The p21 signal was assessed by the nucleus segmentation (*LSetCellTracker* for irradiated cells, watershed segmentation for control group) using the 53BP1 signal after p21 staining, followed by measuring the mean fluorescence signal of p21 in the nucleus. In case of unequal staining intensity of single imaging tiles signal intensity was normalized to overall mean intensity. Threshold for p21-positive cells was defined as the upper 5% of the non-irradiated control population at TP 96 h post irradiation.

Cell segmentation and cell tracking

For nucleus segmentation and cell tracking we used the *LSetCellTracker* tool (information is given below) written in *Matlab*. We performed automated cell-tracking of the imaging data recorded by live-cell imaging in a time interval of approx. 96 h. To assess the quality of tracking we were manually screening for errors in the generated cell division trees. Within this scope, the daughter cells in the last time frame were assigned to the corresponding mother cells (in total 531 mother cells) in the initial time frame of all imaging data acquired using the *wafer architecture*. Approx. 85% of daughter cells were assigned to the corresponding mother cells (including no error in cell division). Approx. 15% of daughter cells were falsely assigned. Approx. 7% of this population were at the transition between correct and miss-assignment.

The variation of 53BP1 expression within the cell population and a close contact of neighboring cells (depending on the seeding number) were identified to be the two main sources of errors. In the latter case neighboring cells were morphologically identified as a single cell. These sources of errors are common issues in cell tracking and are not directly related to the architecture of our biosensor. Optimization of cell tracking could be achieved by using fluorescent 53BP1 constructs with homogenous expression and by applying artificial intelligence or neural network approaches.

To minimize the cell tracking errors, we applied non-supervised and automated cell tracking by *LSetCellTracker* until 25 h after irradiation. For later time points we applied a semi-automatically tracing of cells.

LSetCellTracker

Cell segmentation and tracking are performed using a hybrid algorithm that combines features of both tracking-by-detection and model-based tracking approaches. Cells on the first image of the stack are segmented using the segmentation approach described in (Dzyubachyk et al., 2010). Briefly, this algorithm consists of three core steps: 1. Initial (non-PDE-based) segmentation of the foreground; 2. Splitting the foreground into separate instances (cells); and 3. Refinement of the segmentation by multi-level-set framework. Segmentation of each consecutive image in the stack follows the same logic. However, implementation of the first two steps is different as it relies on the information from the previous TP. Namely, the foreground mask (step 1) is estimated using the threshold that best preserves the foreground region obtained as the final result of the segmentation of the previous image in the stack. An analytic expression for this threshold can be derived using the intensity histogram of the image. Next, to split the foreground into separate regions (step 2), we also use the calculated segmentations of the cells from the previous TP. The foreground is first split into super-pixels, calculated using elliptic features, resulting in an over-segmented image. The super-pixels are consecutively assigned to one of the cells depending on the amount of the overlap between them and regions occupied by each of the cells. In this, detected regions that were not associated with any of the existing cells are labelled as "new" cells and the ones that were not associated with any of the super-pixels are labelled as "disappeared". This process results in a rough segmentation that is subsequently refined using the multi-level-set framework (step 3).

γ-H2AX vs endogenous 53BP1

For the development of the architecture of *Cell-Fit-HD⁴ᴰ* we used the 53BP1 fluorescent damage protein accumulating at DNA damage sites induced by the ion irradiation. 53BP1 is recruited to DSB sites in a slightly delayed fashion compared to γ-H2AX (Vignard et al., 2013). We determined the spatial overlap of the 53BP1- with γ-H2AX signal. In the first step, we determined that 73.9% of the γ-H2AX foci correlate well with 53BP1 foci, both gained by immunofluorescent labelling and confocal microscopy. This discrepancy is most likely explained by high-resolution-dependent detection of spontaneous, short-living yH2AX-foci caused by cell-inherent processes like replication stress.

Expression of 53BP1-mCherry can vary substantially among cells. However, since foci detection occurred in a signal accumulation-dependent manner and with the help of machine learning, which is mainly independent of total intensity, no limitations were expected on that account. Notably, heavy ion irradiation produces complex DSB clusters which directly lead to formation of large, high-intensity RIF (Okayasu, 2012) what minimizes the possibility for missed RIFs. Nonetheless, 53BP1-mCherry-signals were aligned with immunofluorescently stained 53BP1-protein. We determined that 98.8% of large 53BP1 RIF (area >8 pixel) labeled by immunofluorescence overlap with the 53BP1-mCherry foci signal. Here, the identical widefield microscope as for the read-out of the biosensor *Cell-Fit-HD⁴ᴰ* was used.

Microscopy stage movement

We validated the precision of the microscopy stage movement since it has a major impact on the workflow of *Cell-Fit-HD⁴ᴰ* (sew paragraph *wafer architecture*). An identical imaging position was recorded over time in the brightfield mode by WFM (IX83, Olympus) using the *wafer architecture*. A global coordinate system was defined by the *spinels*. Stage movements during sequential imaging of identical positions were computed in a time interval of approx. 72 h. The norm vector of the *spinel* positions (detecting intensity-weighted centroids of the *spinels*) in the maximum intensity projection between two consecutive TPs was computed. The norm vector between the initial and second TP was greater than 1 μm. This parameter decreased rapidly at later TPs. The dimension ($\gg$ 1 μm) of the moving vector at early TPs reflects the needs for the recording of the *initial stack* and consecutive image registration to spatially correlate the ion traversals with cellular information. Neglecting this movement (whether by stage uncertainty or thermal movement and expansion) would result in a degradation of the accuracy in computation of the spatial energy deposition by the ions in the cell layer.

QUANTIFICATION AND STATISTICAL ANALYSIS

Data processing

If not declared otherwise, secondary data processing and statistics were performed using *Matlab* (R2019a).

Ion track reconstruction

The images obtained from the FNTD were analyzed by the software *FNTD package*. This software can be run as a plugin for the image-processing and analysis software *ImageJ/Fiji*. The software is capable of identifying track spots from ions. Based on user input the software can link these track spots together to reconstruct the ion track in the FTND. For the principle of ion track reconstruction using the FNTD read-out signal see (Niklas et al., 2013b). For each series of images obtained, the parameters specified in the *FNTD package* were chosen iteratively in order to maximize the number of tracks found visible on the image stack while minimizing the number of false tracks arising from linking background noise and delta electrons. After the track is reconstructed in 3D in the FNTD, the trajectory was fitted into a line in the 3D space using linear regression in the software *R* (RStudio Team, 2015) and the slope of the trajectory was obtained both in xz and yz directions with error intervals. These slopes were then used to extrapolate the ion tracks into the cell layer at vertical position of 2 μm (thickness of cell layer ∼ 4 μm) with respect to the FNTD surface.

LET and dose calculation

The average intensity of each track was obtained from the *FNTD package*. Distribution of the corresponding track intensities *I* show two distinct peaks which are related to LET of the ion *j* by

$$LET_j = 10^{\frac{I}{a}} - b$$

(Greilich et al., 2018). A Monte Carlo simulation of the ion spectra at the FNTD surface was performed using the *FLUKA* Monte Carlo code. The parameter *a* and *b* were chosen by matching the peaks of the primary (C-12) ion with the Monte Carlo results, while optimizing for total dose by C-12 ions, total number of C-12 ions and the LET distribution of C-12 ions. After the LET of individual ion track was calculated, the dose of each nucleus (*dose_i*) was calculated according to

$$dose_i = \varphi f \times 1.602 \times 10^{-1} \times A_i \times \sum_{j=1}^{n} LET_j$$

with A_i being the cross-sectional area of *nucleus_i* , and φ_f being the fluence factor (Rahmanian et al., 2017). The fluence factor is defined as the fluence of each individual track in the FNTD (as obtained from the *FNTD package*) multiplied by the area scaling factor

(area of the FNTD divided by area of imaging field of the cells), in order to account for the fact that a different area is used to calculate the fluence in the cell layer. To determine the ion traversals $j = 1...n$ for each cell nucleus individually the intersections of the track endpoints with the segmented cross-sectional areas A_i (see below) were calculated. LET and dose calculation were done separately for 1 Gy and 0.5 Gy irradiation. Here, we focused on the dose deposition by primary (C-12) ions. We previously determined in our group that approx. 94% of the energy is deposited by the primary ions (unpublished data). Based on the histogram of the intensity images converted to LET spectrum the primary and secondary ions were distinguished from another by introducing an LET threshold (LET$_{min}$). Expected (from the *FLUKA* Monte Carlo simulation (Dokic et al., 2016)) and reconstructed values are listed in Table S1. We separated the total dose in the entire imaging field defined by the WFM from the reconstructed dose values in the cell nuclei.

In this manuscript the parameters ion hits and dose refer to intranuclear hits and intranuclear dose by C-12 ions.

Correlation of cell response with beam parameters

Raw data were used for the computation of the Pearson-r coefficient and linear regression analysis, meaning that every single cell was represented as a single data point (Figures 2, 3, and S2). Hit numbers, dose and $\sum$LET were limited to maximum 42 hits, 1.3 Gy and 3550 keV/μm to ensure sufficient number of data points. Only initially registered cells were considered for analysis, in contrast to eventual daughter cells.

Assessment of error sources in spatial correlation

Below, we listed all potential sources of errors which principally affect the determination of the correct position of the ion traversal in the cell layer and hence the number of intranuclear hits and computed dose:

- Segmentation error Δs_i of the cell nuclei
- Cell migration Δd_i on the wafer in the time interval between irradiation and initial read-out
- Error Δr_i in registration procedure (including stitching of single imaging tiles),
- Uncertainty Δz_i of the correct vertical position of the cell layer,
- Uncertainty in track reconstruction expressed by the prediction interval $PI_{x,y}$.

Migration Δd_i depends on the cell line. The segmentation error Δs_i strongly depends on the signal intensity of the foreground object including signal decrease at its edges and the segmentation routine applied. Information on the parameters Δz_i and $PI_{x,y}$ and the ion track reconstruction can be found in (Niklas et al., 2013a). The error Δr_i was below 1 μm (see paragraph Stitching and registration procedure above).

We further developed (but did not perform here) a Monte Carlo-based simulation to estimate the total error in the computation of the number of intranuclear hits. The simulation was implemented in *Matlab* and is available online (https://doi.org/10.17632/cdt269pw7m.1).

To determine the error distribution for each individual cell, the simulation was looped with $N = 1000$ for each cell. The algorithm for individual cell nuclei consists of the following steps:

1. Load binary mask BI_i (created by the *LSetCellTracker*) of the maximum intensity projection A_i of nucleus$_i$ in the initial frame after irradiation.
2. Choose a migration distance Δd_i by randomly sampling from a list with migration distances occurring within a time interval of 35 min. Set migration direction by randomly sampling a polar angle φ_i. Shift all foreground pixels by the corresponding translation vector (rounded to integer values).
3. Choose a segmentation error Δs_i of the nucleus by randomly sampling from list with segmentation errors. Depending on the sampling value (over-segmentation, under-segmentation, and correct segmentation) the binary mask BI_i is enlarged or reduced.
4. Define vertical position $\hat{z}$ of the cell layer (maximum intensity projection) with respect to the wafer surface by randomly sampling the corresponding error Δz_i. Select the corresponding track positions and prediction intervals PI_x and PI_y in $\hat{z}$.
5. Recalculate PI_x and PI_y in corresponding normal distribution with $PI_{x/y/y} = 2\,SD_{x/y}$. Compute $\widehat{PI_x}, \widehat{PI_y}$ by sampling from the corresponding normal distribution.
6. Choose registration error Δr_i (rounded to integer values) by randomly sampling from list with the Euclidean distances between the control point pairs. Set translation direction by randomly sampling a polar angle φ_i.
7. Determine all actual track positions (x,y) by translating the track positions in $\hat{z}$ with $\widehat{PI_x}, \widehat{PI_y}$, and Δr_i.
8. Determine number of intersections of track positions (x,y) with the modified binary mask BI_i.

At the end of the simulation the mean number and standard deviation of the distribution of intranuclear hits for each cell nucleus are computed.